The Astrophysical Journal, 928:103 (23pp), 2022 April 1 https://doi.org/10.3847/1538-4357/ac54aa

A Tale of Two Type Ia Supernovae: The Fast-declining Siblings SNe 2015bo and 1997cn

W. B. Hoogendam[1,2], C. Ashall[1], L. Galbany[3,4], B. J. Shappee[1], C. R. Burns[5], J. Lu[6], M. M. Phillips[7], E. Baron[8,9], S. Holmbo[10], E. Y. Hsiao[6], N. Morrell[7], M. D. Stritzinger[10], N. B. Suntzeff[11], F. Taddia[10], D. R. Young[12], J. D. Lyman[13], S. Benetti[14], P. A. Mazzali[15,16], M. Delgado Mancheño[17], R. González Díaz[3,18], and S. Muñoz Torres[17]

[1] Institute for Astronomy, University of Hawaii, 2680 Woodlawn Drive, Honolulu, HI 96822, USA
[2] Department of Physics and Astronomy, Calvin University, Grand Rapids, MI 49546, USA
[3] Institute of Space Sciences (ICE, CSIC), Campus UAB, Carrer de Can Magrans, s/n, E-08193 Barcelona, Spain
[4] Institut d'Estudis Espacials de Catalunya (IEEC), E-08034 Barcelona, Spain
[5] Observatories of the Carnegie Institution for Science, 813 Santa Barbara St., Pasadena, CA 91101, USA
[6] Department of Physics, Florida State University, 77 Chieftan Way, Tallahassee, FL 32306, USA
[7] Carnegie Observatories, Las Campanas Observatory, Casilla 601, La Serena, Chile
[8] Homer L. Dodge Department of Physics and Astronomy, University of Oklahoma, 440 W. Brooks, Rm 100, Norman, OK 73019-2061, USA
[9] Hamburger Sternwarte, Gojenbergsweg 112, D-21029 Hamburg, Germany
[10] Department of Physics and Astronomy, Aarhus University, Ny Munkegade 120, DK-8000 Aarhus C, Denmark
[11] George P. and Cynthia Woods Mitchell Institute for Fundamental Physics & Astronomy, Texas A&M University, Department of Physics and Astronomy, 4242 TAMU, College Station, TX 77843, USA
[12] Astrophysics Research Centre, School of Mathematics and Physics, Queen's University Belfast, Belfast, BT7 1NN, UK
[13] Department of Physics, University of Warwick, Gibbet Hill Road, Coventry, CV4 7AL, UK
[14] INAF—Osservatorio Astronomico di Padova, Vicolo dell'Osservatorio 5, I-35122 Padova, Italy
[15] Astrophysics Research Institute, Liverpool John Moores University, IC2, Liverpool Science Park, 146 Brownlow Hill, Liverpool, L3 5RF, UK
[16] Max-Planck-Institut für Astrophysik, Karl-Schwarzschild Str 1, D-85748 Garching, Germany
[17] Departamento de Física Teórica y del Cosmos, Universidad de Granada, E-18071 Granada, Spain
[18] Instituto Nacional de Astroísica, Óptica y Electrónica (INAOE), 72840 Tonantzintla, Puebla, Mexico
Received 2021 September 12; revised 2022 January 20; accepted 2022 February 10; published 2022 March 30

Abstract

We present optical and near-infrared photometric and spectroscopic observations of the fast-declining Type Ia supernova (SN) 2015bo. SN 2015bo is underluminous ($M_B = -17.50 \pm 0.15$ mag) and has a fast-evolving light curve ($\Delta m15(B) = 1.91 \pm 0.01$ mag and $s_{BV} = 0.48 \pm 0.01$). It has a unique morphology in the observed $V - r$ color curve, where it is bluer than all other supernovae (SNe) in the comparison sample. A ^{56}Ni mass of $0.17 \pm 0.03\,M_\odot$ was derived from the peak bolometric luminosity, which is consistent with its location on the luminosity–width relation. Spectroscopically, SN 2015bo is a cool SN in the Branch classification scheme. The velocity evolution measured from spectral features is consistent with 1991bg-like SNe. SN 2015bo has a SN twin (similar spectra) *and* sibling (same host galaxy), SN 1997cn. Distance moduli of $\mu = 34.33 \pm 0.01$ (stat) $\pm$ 0.11 (sys) mag and $\mu = 34.34 \pm 0.04$ (stat) $\pm$ 0.12 (sys) mag are derived for SN 2015bo and SN 1997cn, respectively. These distances are consistent at the 0.06σ level with each other, and they are also consistent with distances derived using surface-brightness fluctuations and redshift-corrected cosmology. This suggests that fast-declining SNe could be accurate distance indicators, which should not be excluded from future cosmological analyses.

Unified Astronomy Thesaurus concepts: Supernovae (1668)

Supporting material: machine-readable table, data behind figure

1. Introduction

Type Ia supernovae (hereafter SNe Ia) have many astrophysical and cosmological applications. They are one of the major sources of metal enrichment (Raiteri et al. 1996), used as standard candles (e.g., Phillips 1993; Phillips et al. 1999; Burns et al. 2018), and they established the acceleration rate of the universe (e.g., Riess et al. 1998; Perlmutter et al. 1999). SNe Ia have additional applications: they continue to be used to calculate the Hubble constant (e.g., Riess et al. 2016; Burns et al. 2018; Khetan et al. 2021), improve constraints on the equation-of-state for the dark energy w parameter (e.g., Betoule et al. 2014; Scolnic et al. 2018), and investigate the distribution of dark matter in galaxies (e.g., Feindt et al. 2013).

It is apparent that SNe Ia are not an entirely uniform class of objects; rather, there are a growing number of subtypes. These include the overluminous 1991T-like SNe Ia (e.g., Filippenko et al. 1992a; Phillips et al. 1992); 2003fg-like SNe Ia, which are brighter in the near-infrared (NIR) and have long rise times (e.g., Howell et al. 2006; Hicken et al. 2007; Hsiao et al. 2020; Ashall et al. 2021; Lu et al. 2021); 2002cx-like SNe Ia, which show light curves that are both broad and faint (e.g., Li et al. 2003; Foley et al. 2013); 2006bt-like SNe Ia, with the broad, slowly declining light curves seen in high-luminosity SNe Ia, yet lacking a prominent secondary maximum in the i band as seen in low-luminosity SNe Ia (e.g., Foley et al. 2010); 2002ic-like SNe Ia that exhibit Balmer emission lines found in Type IIn core-collapse SNe (Hamuy et al. 2003); and, lastly, 1991bg-like subluminous SNe Ia (e.g., Filippenko et al. 1992b; Leibundgut et al. 1993; Turatto et al. 1996). In addition to these broad categories, there are also several types of SNe Ia that straddle the boundaries between these subtypes. One of

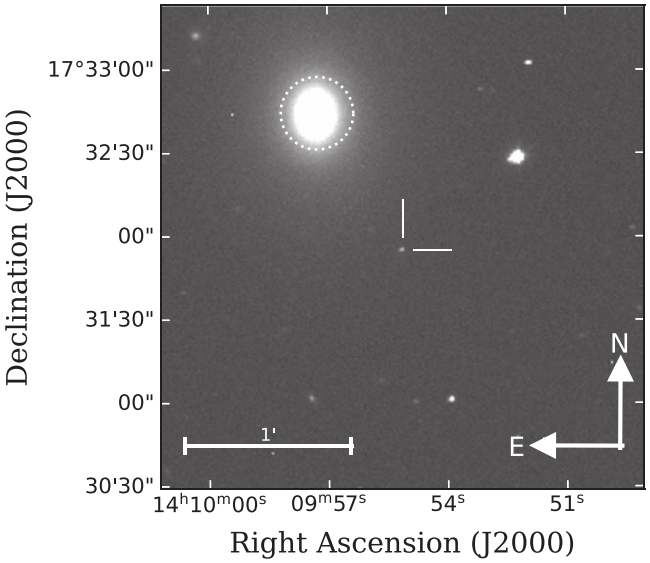

Figure 1. Finder chart for SN 2015bo constructed from an *i*-band image obtained with the Swope telescope on 2015 April 19 at 08:56:55 UT.

these is the so-called transitional SNe Ia. Transitional SNe bridge the gap between normal and 1991bg-like SNe. They tend to be fast declining and exhibit other features of 1991bg-like SNe, but are not entirely consistent with the 1991bg-like SNe classification. Examples of transitional objects include SN 1986G, SN 2003hv, SN 2004eo, SN 2007on, SN 2011iv, iPTF13ebh, and SN 2015bp (e.g., Phillips et al. 1987; Pastorello et al. 2007; Leloudas et al. 2009; Hsiao et al. 2015; Ashall et al. 2018; Gall et al. 2018; Wyatt et al. 2021). For a full review of all subtypes, see Taubenberger (2017).

Roughly 18% of all SNe Ia are considered 1991bg-like SNe (Li et al. 2011). It is hotly debated if they are produced by Chandrasekhar (Ch)-mass or sub-Ch-mass explosions (e.g., Höflich et al. 2002; Stritzinger et al. 2006; Blondin et al. 2018). In addition to being subluminous ($M_B > -18$ mag; Taubenberger 2017), 1991bg-like SNe differ in many ways compared to normal SNe Ia. For example, 1991bg-like SNe light curves differ photometrically with their faster rise and decline and less luminous peak (hence the classification as subluminous). Whereas other SNe have either a shoulder or a second maximum in the *i* band, 1991bg-like SNe have neither (Ashall et al. 2020). However, it is in their spectroscopic properties where 1991bg-like SNe differ the most: they have noticeably stronger Ti II and O I features than other types, and also have a strong Si II feature at 5972 Å (Nugent et al. 1995; Benetti et al. 2005).

One might suspect that, due to their astronomical importance, SNe Ia would be well understood; yet the progenitor systems of SNe Ia, their explosion details, and the underlying physical interpretation of the empirical relationships are not yet fully known despite decades of research. SNe Ia are agreed to come from the explosion of at least one carbon–oxygen (C–O) white dwarf (WD; Hoyle & Fowler 1960). However, there are several potential progenitor scenarios that could produce a SN Ia. These are as follows: the single-degenerate (SD) scenario, which consists of a single C–O WD and a nondegenerate companion star (Whelan & Iben 1973; Livne 1990; Nomoto et al. 1997); the double-degenerate (DD) scenario, which consists of two C–O WDs (Iben & Tutukov 1984; Webbink 1984); and the triple/quaternary scenario, which consists of two C–O WDs in a system with at least one other companion star (Thompson 2011; Pejcha et al. 2013; Shappee & Thompson 2013).

For each of these scenarios, there are a variety of viable explosion mechanisms and ejecta masses. A C–O WD may accrete mass from a companion star until it approaches the Chandrasekhar limit, where compressional heating in the center of the explosion can start a thermonuclear disruption (e.g., Diamond et al. 2018). This can occur in the SD (Whelan & Iben 1973) or DD scenarios (Piersanti et al. 2003). Alternatively, a sub-Ch-mass C–O WD may accrete a surface helium layer which can detonate and produce an inward-moving shock wave and total disruption of the WD (Nomoto 1980; Woosley & Weaver 1994; Hoeflich & Khokhlov 1996). This is possible in both the SD or DD scenarios. A sub-Ch-mass explosion may also result from a merger between two C–O WDs (whose combined mass does not exceed the Chandrasekhar limit; van Kerkwijk et al. 2010). Another explosion mechanism in the DD progenitor scenario is where two WDs violently merge as a result of angular momentum loss from gravitational radiation; the heat generated from merging provides the necessary spark for the powder keg (Iben & Tutukov 1984). Finally, the head-on collision of two WDs, which may be in a multiple system, can possibly produce a SNe Ia where the explosion is triggered by a detonation wave (Raskin et al. 2009; Rosswog et al. 2009; Thompson 2011; Katz & Dong 2012; Kushnir et al. 2013; Pejcha et al. 2013; Dong et al. 2015; Mazzali et al. 2018).

One of the most important empirical relationships that SNe Ia follow is the luminosity–width relationship. This study utilizes the luminosity–width relation in two representations. First, by examining the difference in *B*-band magnitude from maximum light ($t(B)$max) to 15 days past maximum (the Δm15(B) quantity) against the absolute *B*-band magnitude (M_B) (Phillips 1993; Phillips et al. 1999). Second, by examining the time difference between the time of *B*-band maximum and intrinsic $B-V$ maximum normalized by 30 days ($s_{\rm BV}$) versus M_B (Burns et al. 2014). For both of these relationships, more luminous objects have broader light curves; however, $s_{\rm BV}$ is a better indicator for fast-declining objects such as 1991bg-like SNe because Δm15(B) is not a reliable measure of the decline rate for values greater than 1.7 mag (Phillips 2012; Burns et al. 2014; Gall et al. 2018). The physical understanding of the luminosity–width relation lies in the amount of ^{56}Ni synthesized in the explosion (Nugent et al. 1995). More luminous objects produce more ^{56}Ni (Stritzinger et al. 2006), which provides more line opacity and increases the diffusion timescales in the ejecta. This causes broader light curves (e.g., Mazzali et al. 2007). In the case of the least luminous objects, the ^{56}Ni mass will be lower and line opacity small, which causes quickly evolving light curves.

SNe Ia serve as excellent tools to calculate extragalactic distances (Phillips 1993; Hamuy et al. 1996; Phillips et al. 1999) after correcting for the luminosity–width relationship (see Hamuy et al. 1996). However, analyses of distances for SNe Ia in galaxies with low redshifts ($z \leqslant 0.1$) have additional variance due to peculiar velocities and host-galaxy bulk flows relative to cosmological expansion. This can be avoided by comparing SNe Ia that explode in the same galaxy (and thus have the same bulk flow and peculiar velocity), known as "siblings" (Brown 2014). Calculating distances using siblings can also help mitigate systematic uncertainties stemming from

the host-galaxy properties (Kelly et al. 2010; Lampeitl et al. 2010; Sullivan et al. 2010). Additionally, Scolnic et al. (2020) used siblings to investigate correlations between SNe Ia light curves and their host galaxies. Recent studies on SNe Ia siblings include four SNe in NGC 1316 (Fornax A; Stritzinger et al. 2010), SN 2007on and SN 2011iv in NGC 1404 (Gall et al. 2018), SN2013aa and SN 2017cbv in NGC 5643 (Burns et al. 2020), and Biswas et al. (2022) investigated AT 2019lcj and SN 2020aewj.

Fakhouri et al. (2015) introduced the term "twin" SNe. Twins are SNe that show analogous spectral features that imply parallel progenitor scenarios and explosion mechanisms. While Fakhouri et al. (2015) were able to significantly reduce absolute magnitude differences using twins, another study by Foley et al. (2020) found a significant difference in absolute magnitude for the two twins SN 2011by and SN 2011fe. Additionally, SN 2007on and SN 2011iv were also found to be inconsistent with each other despite being in the same galaxy (Gall et al. 2018). SN 1997cn (Turatto et al. 1998) and SN 2015bo are spectrally similar, fast-declining SNe in NGC 5490. The existence of these two SNe presents a rare opportunity to use the power of SN siblings and twins to determine distances that do not suffer from a slew of systematic uncertainties.

In this paper, we present a detailed multiwavelength analysis of the fast-declining SN 2015bo, which is structured as follows. Section 2 presents the data used and a brief analysis of the host galaxy. Light and color curves are derived and compared to other SNe Ia in Section 3. Spectra are presented in Section 4 and compared to several samples of other subtypes of SNe and subluminous SNe. Doppler velocity measurements and pseudo-equivalent-width calculations are also presented in Section 4. In Section 5, we determine the distance to SN 2015bo and compare it to the distance derived from the photometry of SN 1997cn, another fast-declining SN which exploded in the same host galaxy. Final discussion and concluding remarks are offered in Section 6. Throughout this work, phases are reported relative to rest-frame B-band maximum and given values are corrected for foreground galactic extinction.

2. Data

SN 2015bo (a.k.a. PSNJ14095513+1731556) was discovered at $\alpha = 14^{h}09^{m}55^{s}.130$, $\delta = +17°31'55''.60$ by Howerton (2016) on 2015 February 14 at 10:37:06 UT with an apparent V-band magnitude of $m_V = 18.4$ mag. A finder chart for SN 2015bo is presented in Figure 1.

There were two last nondetections: one from the Catalina Real-Time Transient Survey (CRTS; Drake et al. 2009) and the other from the All-Sky Automated Survey for SuperNovae (ASAS-SN; Shappee et al. 2014; Kochanek et al. 2017) on 2015 January 28 at 10:22:17 UT and 2015 February 08 at 13:47:20.40 UT, respectively. Their respective magnitude limits were $m_V = 20.4$ and $m_g = 17.76$. SN 2015bo was classified as a 1991bg-like SNe Ia by the Public ESO Spectroscopic Survey of Transient Objects (PESSTO; Smartt et al. 2015) based on a spectrum taken on 2015 February 15 at 08:29:43 UT (Yaron 2017). It exploded in the type-E galaxy NGC 5490 at a redshift of $z = 0.0161$.[19] The foreground Galactic extinction toward SN 2015bo is $E(B-V)_{MW} = 0.023$ mag (Schlafly & Finkbeiner 2011). Photometric data for SN 1997cn was taken from Jha et al. (2006), and the spectrum in Figure 21 is from Turatto et al. (1998). Spectroscopic data for SN 1997cn are also available from Matheson et al. (2001), Blondin et al. (2012), and Silverman et al. (2012). Table 1 contains properties of both SN 1997cn and SN 2015bo, as well as their host galaxy. In the following subsections, we detail the data for SN 2015bo.

Data for this work comes from two projects: the Carnegie Supernova Project II (CSP-II; Phillips et al. 2019) and PESSTO (Smartt et al. 2015). CSP-II ran from 2011–2015 with the aim of obtaining high-precision follow-up observations of SNe, mainly using telescopes at Las Campanas Observatory. PESSTO's objective was to obtain high-quality spectral observations of transient sources using the European Southern Observatory's New Technology Telescope (NTT) in La Silla.

Table 1
Properties of SN 1997cn, SN 2015bo, and their host galaxy, NGC 5490

Parameters	Value	Reference
SN 2015bo:		
R.A. (J2000)	$14^{h}09^{m}55^{s}.13$	(1)
	212.47971 (deg)	(1)
Decl. (J2000)	$+17°31'55''.60$	(1)
	17°.53211	(1)
$t\,(B)_{max}$ (JD)	2457078.3 ± 0.1 (day)	This work
M_B[a]	−17.50 ± 0.15 (mag)	This work
$E(B-V)_{MW}$	0.023 (mag)	(2)
$E(B-V)_{Host}$	0.00 ± 0.00 (mag)	This work
s_{BV}[b]	0.48 ± 0.01	This work
Δm15(B)[c]	1.91 ± 0.01 (mag)	This work
SN 1997cn:		
R.A. (J2000)	$14^{h}09^{m}57^{s}.76$	(7)
	212.49067 (deg)	(7)
Decl. (J2000)	$+17°32'32''.32$	(7)
	+17°.54231	(7)
$t\,(B)_{max}$ (JD)	2450588.3 ± 0.1 (d)	This work
M_B[e]	−17.43 (mag)	This work
$E(B-V)_{MW}$	0.023 (mag)	(2)
$E(B-V)_{Host}$	0.03 (mag)	(7)
s_{BV}[a]	0.35 ± 0.06	This work
Δm15(B)[c]	1.90 ± 0.05 (mag)	(7)
NGC 5490:		
Type	Elliptical	(3)
R.A. (J2000)	$14^{h}09^{m}57^{s}.295$	(4)
	212°.488728	(4)
Decl. (J2000)	$+17°32^{m}43^{s}.98$	(4)
	17°.545551	(4)
Velocity, v	12 km s^{-1}	(5)
z_{helio}	0.0161 ± 0.0001	(6)
μ[d]	34.21 ± 0.15 (mag)	(6)

Notes.
[a] Corrected only for Galactic extinction using $R_V = 3.1$.
[b] Obtained using a Gaussian process fit in SNooPY.
[c] Obtained using direct Gaussian process interpolation to the B band.
[d] Corrected to the cosmic microwave background rest frame and calculated using $H_0 = 73$ km s^{-1} Mpc^{-1}, $\Omega_m = 0.27$, and $\Omega_\Lambda = 0.73$, which is used throughout this work.
[e] This value is from light-curve models fit to the data rather than directly from the data.
References: (1) Howerton (2016); (2) Schlafly & Finkbeiner (2011); (3) de Vaucouleurs et al. (1991); (4) Adelman-McCarthy et al. (2008); (5) Simien & Prugniel (1997); (6) Kowalski et al. (2008); (7) Jha et al. (2006).

[19] van den Bosch et al. (2015) from ned.ipac.caltech.edu.

2.1. Photometric Observations

Photometric observations were acquired in the *uBVgriJHY* filters from −6.9 days to +105.8 days relative to rest-frame *B*-band maximum light. Optical photometry was obtained from the Swope telescope, and the NIR photometry came from the du Pont Telescope. Both telescopes are located at the Las Campanas Observatory. All photometric measurements are presented in the natural system and reduced using the methods described in Krisciunas et al. (2017) and Phillips et al. (2019). Logs of the optical and NIR observations are presented in Appendix B. Host-galaxy template subtraction was not required for SN 2015bo as it is located far away from the center of the host at ∼20 kpc. Derived maximum apparent magnitudes in each CSP filter and their corresponding times relative to $t(B)$max are presented in Table 2.

2.2. Spectroscopic Observations

Sixteen optical and one NIR spectra of SN 2015bo were obtained from −7.8 days to +31.8 days relative to rest-frame *B*-band maximum light. Spectra were taken with a variety of instruments including SPRAT mounted on the Liverpool Telescope, ALFOSC on the Nordic Optical Telescope, EFOSC on the NTT, and WFCCD on the du Pont Telescope. The optical spectra were reduced using the standard IRAF[20] packages and methods described in Hamuy et al. (2006), Folatelli et al. (2013), and Smartt et al. (2015). The NIR spectrum was obtained with the Folded-port InfraRed Echellette (FIRE) on the Baade telescope at the Magellan Observatory and reduced using the methods described in Hsiao et al. (2019). Table 3 presents a summary of the spectral data.

2.3. Host Galaxy

Integral-field spectroscopy of NGC 5490 was obtained on 2021 January 27 08:04:06, with the Multi-Unit Spectroscopic Explorer (MUSE; Bacon et al. 2010). MUSE is mounted on the Unit 4 telescope at the ESO Very Large Telescope at the the Cerro Paranal Observatory. These host observations were obtained as part of the All-weather MUSE Supernova Integral-field Nearby Galaxies (AMUSING; Galbany et al. 2016; López-Cobá et al. 2020) survey. AMUSING is an ongoing project that analyzes the host galaxies of SNe to study their environments.

Figure 2 presents a synthetic *r*-band image extracted from MUSE observations of the host galaxy. SN 2015bo is distant from the center of the host galaxy, NGC 5490. This suggests that host-galaxy extinction is minimal for SN 2015bo. The object adjacent to SN 2015bo is an unrelated background galaxy.

3. Photometry

3.1. Light Curves

The multiband *uBVgriJHY* light curves are presented in Figure 3. The filters are organized top-down from blue wavelengths to red wavelengths. Data from five optical filters (*BVgri*) extend to ∼+80 days after the time of *B*-band maximum ($t(B)$max). *BVg* rise on timescales longer than ∼10 days, but the true time of explosion is uncertain as the last nondetections are not constraining.

[20] IRAF is distributed by the National Optical Astronomy Observatory, which is operated by the Association of Universities for Research in Astronomy, Inc., under cooperative agreement with the National Science Foundation.

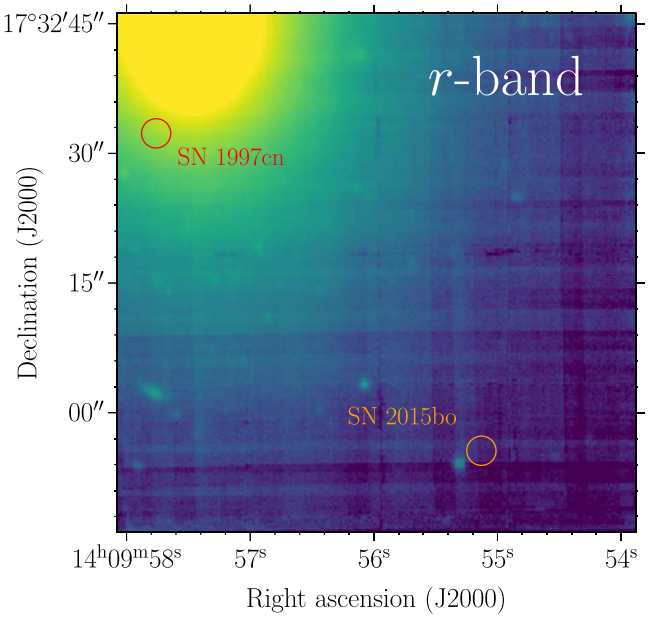

Figure 2. The MUSE data cube synthetic *r*-band image. The image was obtained by convoluting the spectra by an *r*-filter transmission. The orange and red circles represent a 1 kpc^2 aperture centered on the positions of SN 2015bo and SN 1997cn, respectively.

To derive important photometric quantities such as $t(B)$max, maximum m_B, and $\Delta m15(B)$, we utilize the SuperNovae in object-oriented Python (SNooPy; Burns et al. 2011, 2014) template light-curve fitting software package.[21] The *B* band was interpolated using a Gaussian process technique which underwent 150 Monte Carlo iterations to determine the uncertainties. The 1σ deviation from the Monte Carlo iterations was used as the uncertainty for the derived values. We used the 1991bg-like SN spectral energy distribution (SED) template within SNooPy[22] to perform *K*-corrections. This correction template is used throughout this work for fitting fast decliners with SNooPy. Light-curve parameters of $t(B)\text{max} = 2457078.3 \pm 0.1$ day and maximum $m_B = 16.83 \pm 0.01$ mag were computed. $\Delta m15(B)$ and s_{BV} were calculated using the same direct Gaussian process interpolation technique. To calculate s_{BV}, only data with both *B* and *V* bands taken on the same night were used. The values of $\Delta m15(B)$ and s_{BV} are 1.91 ± 0.01 mag and 0.48 ± 0.01, respectively. Derived maximum apparent magnitudes in each CSP filter and their corresponding times relative to $t(B)$max are presented in Table 2. The *u*-band peaks ∼2 days prior to $t(B)$max, whereas the *V*, *g*, *r*, and *i* bands all peak after $t(B)$max. Throughout this work we use the parameters derived from the Gaussian process interpolation unless otherwise stated.

To assess if SN 2015bo is a "normal" 1991bg-like SNe, we fit the multiband light curves with the EBV2 model in SNooPy. Interestingly, the fits determine $E(B-V)_{\text{Host}} = 0.21 \pm 0.01$ (stat) $\pm$ 0.06 (sys). However, no narrow Na I lines were seen in the spectra. An upper limit on the on Na I pseudo-equivalent width was calculated using the method described in Ashall et al. (2021). Using the method of Poznanski et al. (2012) between Na I D pseudo-equivalent width and $E(B-V)$ produced an upper limit of $E(B-V)_{\text{Host}} = 0.02 \pm 0.02$ mag, where the uncertainty was determined via the method of

[21] https://csp.obs.carnegiescience.edu/data/snpy

[22] Taken from https://c3.lbl.gov/nugent/nugent_templates.html.

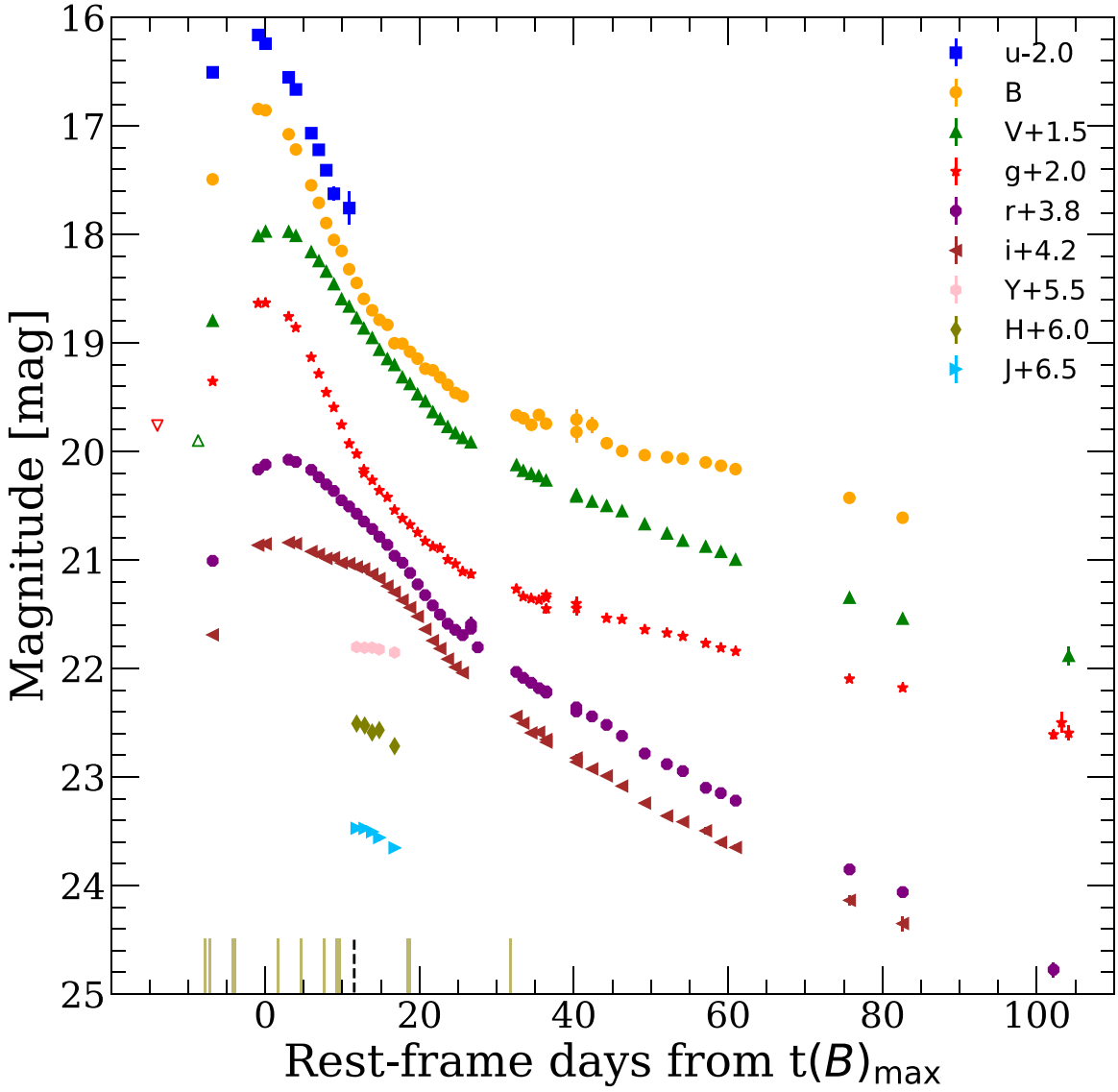

Figure 3. Rest-frame optical and near-IR (NIR) photometry of SN 2015bo. The *V*-band discovery point is given as a green, upward open triangle. The last nondetection from ASAS-SN in the *g* band is provided as a red, downward open triangle. Solid, dark khaki lines on the bottom horizontal axis represent epochs with optical spectra, and the dashed black line represents the epoch of our NIR spectrum.

Table 2
Table of Maximum Light Apparent Magnitudes

Filter CSP-II	Magnitude (mag)	σMagnitude (mag)	$t_{max} - t(B)$max (days)	σt_{max} (days)
u	18.15	0.01	−1.9	0.3
B	16.44	0.01	0.0	0.1
V	16.84	0.01	2.0	0.1
g	16.62	0.01	0.6	0.1
r	16.27	0.01	2.7	0.1
i	16.62	0.01	2.1	0.1
H[a]	16.51	0.04	12.9	1.3

Note.
[a] The *H* band was the only near-IR (NIR) band where SNooPy was able to derive a maximum value. This is likely due to the lack of data in the NIR regime.

Phillips et al. (2013). Additionally, SN 2015bo is far away from its elliptical host galaxy, reducing the chance of significant host-galaxy extinction. We conclude that the host-galaxy extinction must be minimal, and that the SNooPY fits are inaccurate in this area of the parameter space. Therefore, throughout this work we opt to not correct for host-galaxy extinction.

To determine the distance modulus to SN 2015bo, we use the SNooPy EBV2 model with the prior that the host-galaxy extinction, $E(B-V)_{\rm Host} = 0$ mag. A distance modulus of $\mu = 34.33 \pm 0.01$ (stat) ± 0.11 (sys) mag was derived. Further discussion about distance calculations and a more accurate derivation of the distance modulus and its systematic uncertainty can be found in Section 5. The SNooPy fits (see Figure 4) show that SN 2015bo's photometry is well matched by 1991bg-like SNe light-curve templates.

Figure 5 compares the light curves of SN 2015bo in *BVgri* with a selection of subtypes of SNe Ia from CSP-II. SN 2015bo's light curve resembles 1991bg-like SNe, and it evolves more quickly than the other types of SNe Ia in every band except the *i* band. The lack of a distinctive knee-type feature in the *r* band when compared to normal and 1991T-like SNe highlights this difference. The broader *i* band can be used

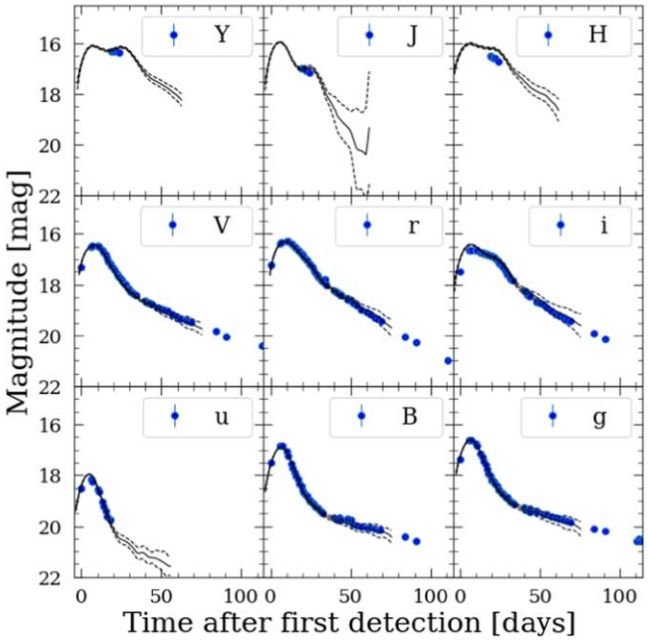

Figure 4. SNooPy fits described in Section 3.1. These fits are produced with the EBV2 model and the prior that the host-galaxy extinction is 0 mag. The vertical axis is plotted in magnitudes, and the horizontal axis is in days after the first data point.

to confirm if a SN is a subluminous SN. SN 2015bo, like many other subluminous SNe, lacks a secondary *i*-band maximum, whereas normal and 1991T-like SNe have a distinct secondary maximum. In normal SNe Ia, the secondary *i*-band maximum comes from recombination of iron-group elements (Höflich et al. 2002; Kasen 2006; Jack et al. 2015); however, in 1991bg-like SNe, Kasen (2006) and Blondin et al. (2015) propose the recombination either does not occur or occurs earlier, which causes the maxima to merge and appear as one maximum in the light curve. This is also why the *i*-band peak occurs after the *B*-band maximum. The importance of the second *i*-band maximum for using SNe Ia as distance indicators is discussed in Section 5. The *i* band for SN 2015bo is also slightly broader than the 1991bg-like SNe comparison sample. Interestingly, SN 2015bo shows some similarities with 2002cx-like SNe in the *Bgr* bands, but SN 2015bo declines significantly faster than 2002cx-like SNe in the *Vi* bands. Although 2003fg-like SNe show a somewhat wider variety in their light-curve morphologies, it is still evident that SN 2015bo declines more quickly than all 2003fg-like SNe in all plotted filters, and for most 2003fg-like SNe this difference in decline rate is significant.

Ashall et al. (2020) showed SNe Ia can be photometrically subtyped by just their $s_{\rm BV}$ value and their time of primary *i*-band maximum relative to *B*-band maximum $t(i-B_{\rm max})$. Figure 6 presents this relationship with SN 2015bo overlaid. SN 2015bo is located in the 1991bg-like SNe area of the parameter space where there are fewer SNe. This suggests the classification that SN 2015bo is a 1991bg-like SN.

3.2. Color Curves

In Figure 7, the color curves of SN 2015bo are presented. Throughout this work, we use *K*-corrected intrinsic colors. Color curves are obtained by subtracting photometric points observed on the same night. No interpolations between data points were performed. At early times, the color is a diagnostic of the temperature of the photosphere, so Figure 7 provides an approximate measurement of the temperature over time. Both the $B-V$ and the $g-r$ color curves are similar: they exhibit sharp increases from bluer to redder from $\sim$0 day to $\sim$+15 days and then turn to become bluer after $\sim$+15 days; however, $g-r$ declines more quickly than $B-V$ over this time frame. After $\sim$+55 days, the photosphere is well within the ejecta and the color no longer measures the temperature but rather differences in ionization state from a mixture of absorption and emission features. At later epochs, $B-V$ flattens off to eventually reach a value of $\sim$0.5 mag at $\sim$+80 days, whereas $g-r$ continues to decline as far out as $\sim$+100 days to reach a value of ~-0.4 mag. The $V-r$ color curve also peaks near $\sim$+15 days, but it does not rise as steeply as $B-V$ or $g-r$. When it declines, $V-r$ is broader than $g-r$ and is approximately the same slope as $B-V$. The $r-i$ color curve displays a slightly later red peak at around +20 days rather than around +15 days, and it also has a noticeably less steep increase; it also flattens off over time rather than declines. The flattening starts at $\sim$+30 days, which is earlier than when the $B-V$ color curve may start to flatten in the last two $B-V$ data points. These color-curve shapes are abnormal; they may provide a potential explanation as to why the SNooPy EBV2 model wants to have a larger extinction value than can be derived from the Na I D equivalent width.

Figure 8 compares the intrinsic color curves of SN 2015bo to a variety of other SNe Ia. The comparison SNe Ia are corrected for both their respective Galactic and host-galaxy extinctions. SN 2015bo is plotted in black diamonds, with two transitional SNe Ia, SN 2007on and SN 2011iv, plotted in blue circles and red squares, respectively. These two transitional objects are plotted individually because they also exhibit the same peculiar blue rise in the $r-i$ color curve that SN 2015bo has after $\sim$+40 days (see below for details). SN 2007on and SN 2011iv are interesting objects in their own right: they both exploded in NGC 1404, and they are both transitional SNe Ia. Detailed discussions of SN 2007on and SN 2011iv can be found in Gall et al. (2018) and Ashall et al. (2018).

In $B-V$, SN 2015bo starts bluer than the comparison sample and becomes more red that the comparison sample over time after $\sim$+30 days. Its Lira tail (the region in the $B-V$ color curve after $\sim$+20 days for which the majority of SNe have similar slopes; Phillips et al. 1999) is the steepest of our sample. Comparing SN 2007on and SN 2011iv, Gall et al. (2018) found SN 2011iv was bluer earlier on, yet it became redder than SN 2007on at $\sim$+30 days. Gall et al. (2018) interpreted this as an effect from the progenitor WDs having differing central densities at the time of explosion. Therefore, the ^{56}Ni distributions would be different for SN 2007on and SN 2011iv. At *B*-band maximum and at the reddest color inflection point, SN 2015bo has a similar $B-V$ color to SN 2007on; however, the slope of the decline in the Lira tail is steeper in SN 2015bo than both SN 2007on and SN 2011iv. This could be an indication that the central density of SN 2015bo is even lower than SN 2007on.

The $V-r$ color curve for SN 2015bo is unique. It reaches a red peak higher than any other observed SN Ia in our comparison sample. This is peculiar, especially considering this same behavior does not occur in either $r-i$ or $B-V$ colors, or with other transitional or 1991bg-like SNe. Additionally, it

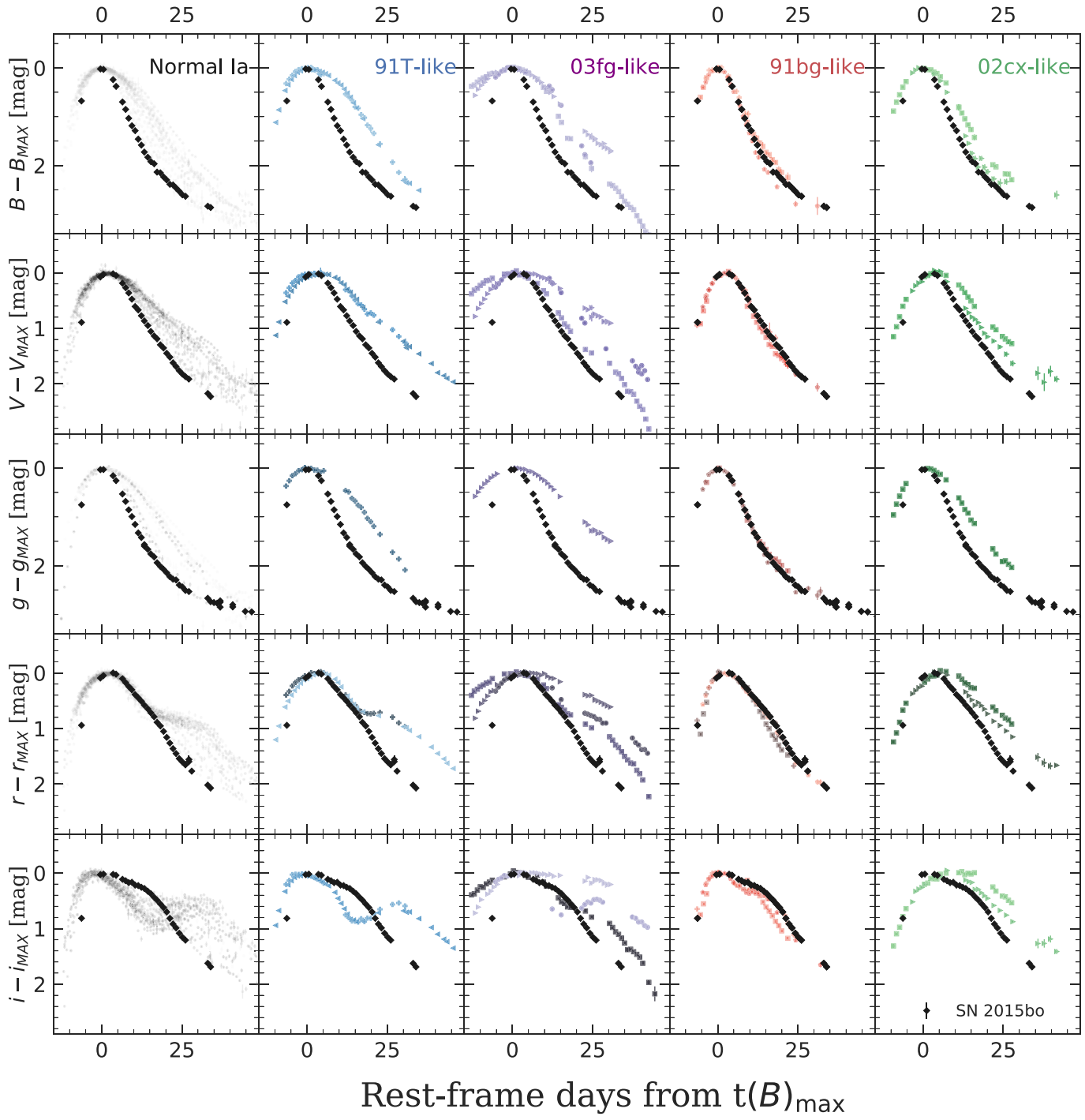

Figure 5. The *B*-band (first row), *V*-band (second row), *g*-band (third row), *r*-band (fourth row), and *i*-band (fifth row) light curves compared to a selection of SNe Ia subtypes: normal (first column/gray), 91T-like (second column/blue), 03fg-like (third column/purple), 91bg-like (fourth column/orange), and 02cx-like (fifth column/green). SN 2015bo (black points) deviates significantly from all other types of SNe Ia, but matches quite well with other 1991bg-like SNe. Comparison SNe are from Ashall et al. (2020).

seems that the triumvirate of SN 2007on, SN 2011iv, and SN 2015bo decline in $V - r$ more rapidly than normal SNe Ia after $\sim$+50 days past $t(B)$max.

Another intriguing property of SN 2007on, SN 2011iv, and SN 2015bo is the redward rise of the $r - i$ color curve at $\sim$+40 days after *B*-band maximum. This red color shift could be due to the fact that fast decliners are [Ca II] strong. Therefore the [Ca II] $\lambda\lambda$ 7291.5, 7323.9 emission, which is usually seen beginning at $\sim$+40 days (Taubenberger 2017), will affect the $r - i$ color curve. This difference in the $r - i$ color curve after $\sim$+40 days could provide a robust way to photometrically distinguish a subset of transitional and/or 1991bg-like SNe that may share a progenitor scenario or explosion mechanism or to distinguish fast-declining SNe from normal SNe Ia.

The $r - i$ color minimum that occurs just after $t(B)$max for SN 2007on, SN 2011iv, and SN 2015bo are also significantly earlier and bluer than normal SNe Ia. This earlier first turning point could provide a good way to identify subluminous SNe Ia

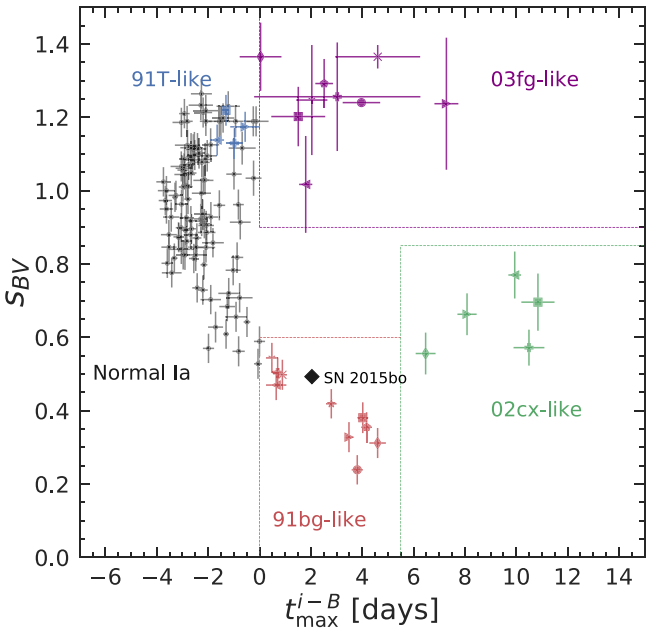

Figure 6. The color stretch parameter s_{BV} as a function of time difference between i- and B-band maxima, t_{max}^{i-B}. Different subtypes of SNe Ia occupy different areas of the plot, as shown in Ashall et al. (2020).

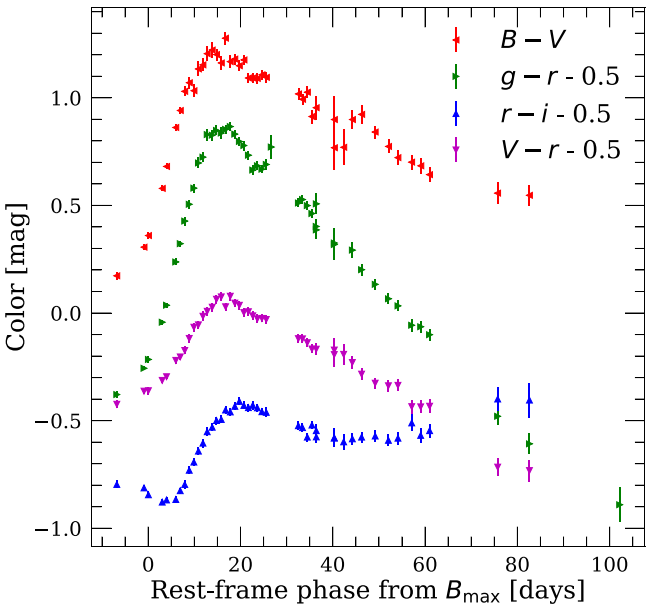

Figure 7. Color vs. rest-frame days from B_{max} for SN 2015bo. From top to bottom, plotted colors are $B-V$ (red), $g-r$ (green), $V-r$ (magenta), and $r-i$ (blue). Color curves have been corrected for Milky Way, but not host-galaxy, extinction.

in future studies. We see no evidence for an inflection point at ∼0–10 days in the $V-r$ color despite having data during the epochs where all other SNe Ia in the sample turn.

3.3. Luminosity–Width Relation

The peak absolute magnitude of SN 2015bo is calculated from the light curves to be $M_B = -17.50 \pm 0.15$ mag. This value has been corrected for only foreground extinction and not host-galaxy extinction. This absolute magnitude is derived using the cosmic microwave background (CMB)-corrected distance modulus, which is 34.21 ± 0.15 mag.

The luminosity–width relation is plotted in Figure 9 using comparison SNe from the CSP-I and CSP-II. SN 2015bo is plotted without corrections for host-galaxy extinction, and the rest of the sample is corrected for host-galaxy extinction. The left side of the figure is for the B band, whereas the right side of the figure is for the V band. SN 2015bo is located with the transitional and 1991bg-like SNe and is within the area of parameter space $s_{BV} \approx 0.5$, where there is a lack of objects (Ashall et al. 2016). The background-comparison SNe in the left panels of the Figure use absolute magnitude values from SNooPy template fits using the EBV2 model; the comparison SNe in the background-comparison SNe in the right panels use M_V and $\Delta m15(V)$ from direct Gaussian process fits with the same method as in Section 3.1. This explains the difference in scatter between the luminosity–width relation in the B band compared to the V band.

In the top-left panel, SN 2015bo is located in the degenerate region of the luminosity–width relation parameter space. This degeneracy arises from $\Delta m15(B)$ obtaining the same value for different light-curve shapes (Burns et al. 2014). However, when the correlations are plotted as a function of s_{BV}, SN 2015bo occupies the bright end of the 1991bg-like SNe parameter space in the luminosity–width relation. In the B band, M_B is among the parameter space occupied by other fast decliners. In the V band, SN 2015bo is in the fast-declining, underluminous parameter space, as well.

SN 1997cn is also plotted in Figure 9 using the photometry from Jha et al. (2006). Due to the photometry starting well after maximum in all bands, we were unable to directly calculate the time of B- or V-band maxima, maximum magnitudes in the B and V bands, $\Delta m15(B)$, $\Delta m15(V)$, or s_{BV}. Because of this, values from the best-fit templates derived from the SNooPy EBV2 model were used for SN 1997cn. In all panels, SN 1997cn occupies the same parameter space as SN 2015bo.

3.4. Bolometric Light Curves

Pseudo-bolometric light curves were constructed using the direct SED method within SNooPy. The wavelength range was from 3000 to 19370 Å. In short, the method converts the magnitudes into fluxes to produce a SED, the 1991bg-like spectral templates are used for K- and S-corrections, and the SED is integrated and scaled with respect to the distance modulus to produce a bolometric flux at each epoch. Due to the lack of temporal coverage in the infrared data, we used a Rayleigh–Jeans model to extrapolate our SEDs when data was not available. The SEDs were also corrected for Milky Way extinction. The error on the bolometric light curve was determined via varying the distance modulus through 100 Monte Carlo iterations. To do this, the distance modulus was treated as a Gaussian distribution. A Gaussian process was used to determine the maximum for each iteration. The mean value of these maxima from the Monte Carlo iterations was taken as the final peak pseudo-bolometric luminosity, and the mean of the standard deviations of the maxima was taken as the uncertainty.

The peak pseudo-bolometric luminosity of SN 2015bo is $L_{bolo}^{peak} = 0.33 \pm 0.03 \times 10^{43}$ erg s^{-1}. Using the relation between L_{bolo}^{peak} and ^{56}Ni mass presented in Stritzinger & Leibundgut (2005) and Arnett (1982), a ^{56}Ni mass of 0.17 ± 0.05 $M_\odot$ is derived. Calculated values are compared to other SNe Ia presented in Ashall et al. (2018) in Figure 10. Both the bolometric luminosity and ^{56}Ni mass of SN 2015bo

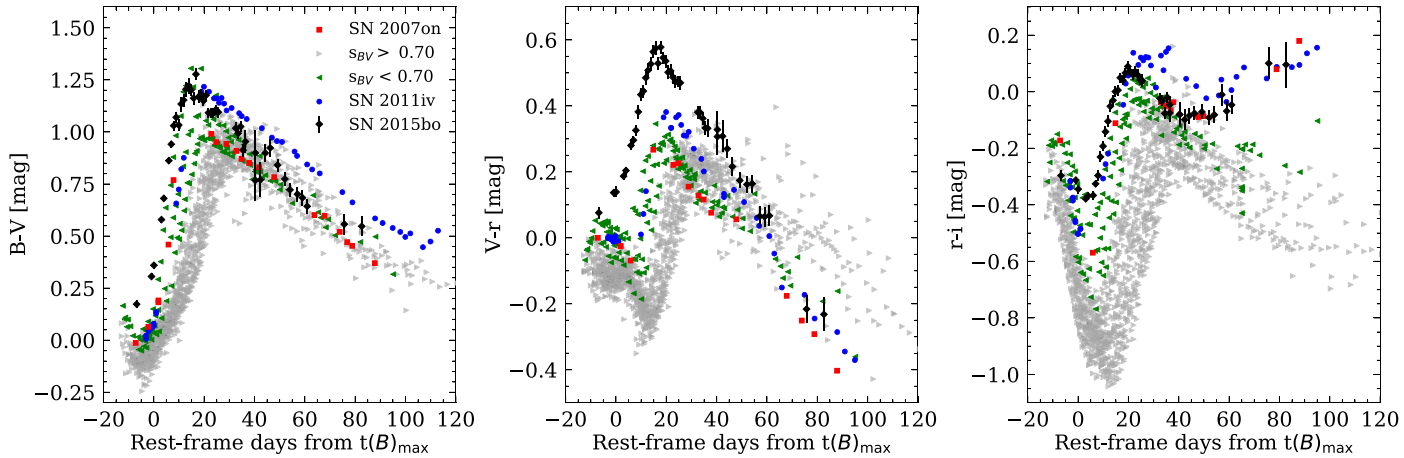

Figure 8. Comparison of intrinsic color curves for SN 2015bo and other SNe. Plotted colors from left to right are $B - V$, $V - r$, and $r - i$. SN 2015bo is plotted in black diamonds with two similar SNe Ia, SN 2007on and SN 2011iv, plotted in blue circles and red squares, respectively. Green, left-facing triangles are other fast decliners; the condition $s_{BV} < 0.70$ effectively segregates between normal and fast-declining SNe Ia. Grey, right-facing triangles are all other types of SNe Ia. All comparison SNe Ia data points have been corrected for both Milky Way and host-galaxy extinction, whereas SN 2015bo is only corrected for Galactic extinction since there is most likely an insignificant amount of host-galaxy extinction.

are consistent with the general trend presented in Ashall et al. (2019a). SN 2015bo has a lower luminosity and lower ^{56}Ni mass than the majority of the CSP comparison sample. This places it near other 1991bg-like SNe.

A similar pseudo-bolometric light curve and ^{56}Ni mass were not computed for SN 1997cn because the data for SN 1997cn is insufficient to directly derive a ^{56}Ni mass. However, Turatto et al. (1998) found a ^{56}Ni mass of $\sim$0.1 $M_{\odot}$for SN 1997cn using spectral models.

4. Spectra

Photometry is a powerful tool for classifying and studying SNe, but it does not reveal the full picture. Spectroscopic observations complement photometric ones and enable further understanding of the elemental composition of SNe. Due to the homologous ($v \propto rt$) expansion of a SN ejecta $\sim$10 s after the explosion, obtaining a time series of spectra allows the reconstruction of the evolution of the ejecta over time. In addition to providing composition information, spectra also can be used to derive velocities of the ejecta and provide additional information on the physics of the explosion such as the temperature, the ionization state, and the kinetic energy.

4.1. Optical Spectra

Figure 11 presents a time series of the optical spectra compiled here for SN 2015bo. The spectra span from -7.8 days to $+31.8$ days relative to B-band maximum. The spectra are dominated by features of intermediate-mass and Fe-group elements as well as oxygen. The main spectral features we identify are as follows: Ca II H&K $\lambda\lambda$ 3968, 3933, Ti II λ4395, Fe II $\lambda\lambda$ 4923, 5169, Fe III λ5156, S II $\lambda\lambda$ 5449, 5623, Si II $\lambda\lambda$ 5972, 6355, O I λ7774, and Ca II $\lambda\lambda$ 8498, 8542, 8662 NIR lines. These lines are identified based on Mazzali et al. (1997) and Ashall et al. (2016).

Spectra of SN 2015bo are compared to other subtypes of SNe Ia at maximum light and $+20$ days in Figure 12. All objects in the sample are dominated by intermediate-mass elements (IMEs) and Fe-group elements. Most have a strong Si II λ6355 feature. SN 2015bo is most similar to SN 1991bg, as demonstrated by the strong Si II λ 5972 feature. In other SNe, the Si II λ5972 feature is weak or entirely absent (e.g., SN 1991T and SN 2011fe). While not as strong as SN 1991bg, SN 2015bo's Ti II λ4400 feature is still present. This feature (Ti II λ4400) is only observed in our sample in SN 2015bo, SN 1991bg, and SN 2006bt. As the strength of the Si II λ5972 and Ti II λ4400 is indicative of temperature, this suggests SN 2015bo has a photospheric temperature between those of SN 1991bg and a normal Ia such as SN 2011fe. By $+20$ days, all of the SNe in the sample look similar because the photosphere is well within the ^{56}Ni region.

Figure 13 compares SN 2015bo to other SN 1991bg-like and transitional SNe Ia. The sample is arranged by s_{BV} value; there is a trend that SNe with smaller s_{BV} have stronger Si II λ5972 features. The Ti II λ4400 feature also shows the same relationship between depth and s_{BV}. Within this trend, SN 2015bo is located between SN 2005bl and SN 1986G both in terms of s_{BV} and the strength of the Ti II λ4400 and Si II λ5972 features. Figures 9 and 10 confirm this: in both plots, SN 2015bo resides on the more luminous end of the fast decliners. These photometric results are consistent with spectral observations. SN 1997cn is also plotted to compare its spectra to the other SNe; it falls between SN 2005bl and SN 1991bg based on s_{BV} value.

Discussing spectral differences in a qualitative manner is helpful to see general trends; however, as a scientific method it is imprecise. Therefore, velocities and pseudo-equivalent widths are derived to provide a quantitative picture of SN 2015bo and its spectral relationship to other SNe Ia. These measurements are presented in Section 4.3.

4.2. Velocity and Pseudo-equivalent-width Fitting Method

We fit all optical spectra using the Measure Intricate Spectral Features In Transient Spectra[23] (mistfits; S. Holmbo et al. 2022, in preparation) fitting program. This program was used to calculate both the wavelengths of each spectral feature and the pseudo-equivalent widths. To fit the wavelengths, spectra were smoothed using misfits' low-pass fast-Fourier-transformed filter spectra following the method described in Marion et al. (2009). An uncertainty spectrum was computed from the difference between the observed and smoothed spectra. The

[23] https://github.com/sholmbo/misfits

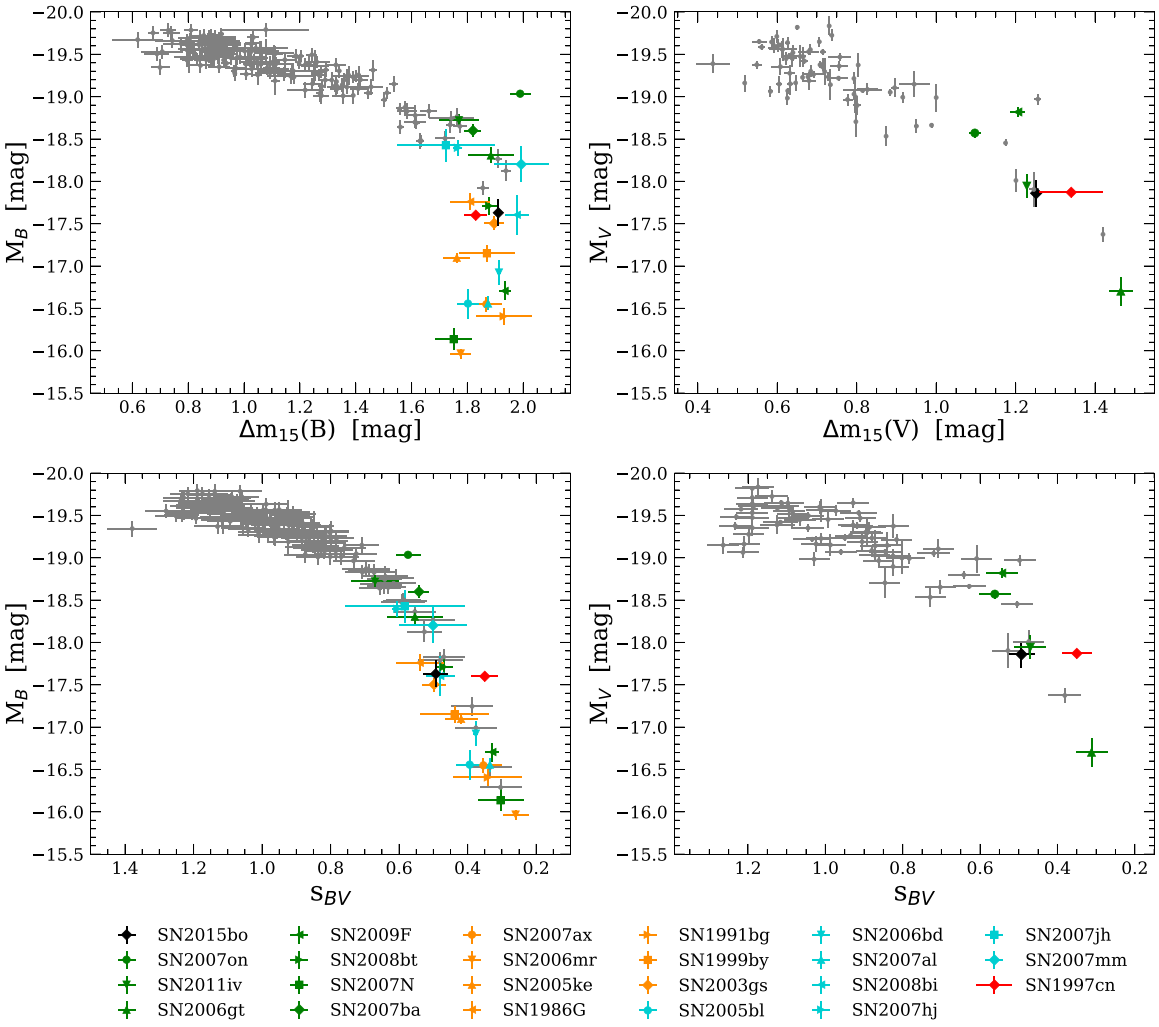

Figure 9. Luminosity–width relation using $s_{\rm BV}$, Δm15(B), and Δm15(V). For all panels, the black diamond is SN 2015bo. The absolute magnitude for SN 2015bo was computed without host-galaxy extinction (i.e., $E(B-V)_{\rm Host}=0.00$). The $s_{\rm BV}$ and peak magnitude for SN 2015bo were both calculated with a direct Gaussian interpolation. Other fast decliners are plotted as green, orange, or cyan diamonds, triangles, and squares. SN 1997cn is plotted as the red diamond. Grey points are a sample of other subtypes and normal SNe Ia. Top left: absolute B-band magnitude plotted against Δm15(B). Bottom left: absolute B-band magnitude plotted against $s_{\rm BV}$. Top right: absolute V-band magnitude plotted against Δm15(V). Bottom right: absolute V-band magnitude plotted against $s_{\rm BV}$. For the background SNe Ia on the left-hand side, $s_{\rm BV}$ and Δm15(B) values come from the EBV2 model within SNooPy, whereas on the right-hand side $s_{\rm BV}$ and Δm15(V) values for the background SNe Ia are directly computed by SNooPy using a direct Gaussian interpolation on the specific band. All background SNe satisfy the following: $z>0.01$, $A_V<0.75$ mag, $\sigma M_V<0.3$ mag, $\sigma\Delta{\rm m}_{15}({\rm V})<0.05$ mag, and $\sigma s_{\rm BV}<0.05$. These choices were made to eliminate poorly measured background SNe or objects that suffered from significant extinction and/or uncertain distances due to peculiar velocities.

absolute values of the residuals were smoothed using a Gaussian filter where the smoothed residuals contain 68% of the absolute value of the residual level. This is used as the 1σ error spectrum.

From there, a Gaussian function and a linear continuum were simultaneously fitted to each feature using the *velocity. gaussians* function within misfits. The initial guess continuum boundary points were selected by hand, and the best fit was determined by χ^2 minimization. A final wavelength and uncertainty were respectively determined using the mean and standard deviation of 1000 Monte Carlo iterations. This uncertainty was added in quadrature with the uncertainty of the instrument resolution to arrive at the final wavelength uncertainty. The relativistic Doppler formula and rest wavelength of the feature were used to convert the wavelength of the absorption minimum into velocities.

Pseudo-equivalent-width determination followed the procedure presented in Garavini et al. (2007) using misfits' *width. shallowpew* function. The mean and standard deviation of 1000 Monte Carlo iterations were used as the pseudo-equivalent width value and 1σ uncertainty.

4.3. Branch Diagram, Velocities, and Pseudo-equivalent Width

4.3.1. Branch Diagram

An additional way to classify SNe Ia into subtypes is to plot the pseudo-equivalent width (pEW) of Si II λ5972 against Si II λ6355 at maximum (Branch et al. 2006). Figure 14 shows SN 2015bo along with other SNe Ia. There are four regions: Shallow Silicon, Core Normal, Cool, and Broad Line. Core Normal SNe are a highly homogeneous group with similar spectral features. Broad Line SNe are similar to Core Normal, but have broader features. Likewise, Shallow Silicon are also similar to Core Normal but tend to have equally weak Si II λ5972 and Si II λ6355 features. Shallow Silicon SNe tend to be overluminous. Finally, there are the Cool SNe. These objects

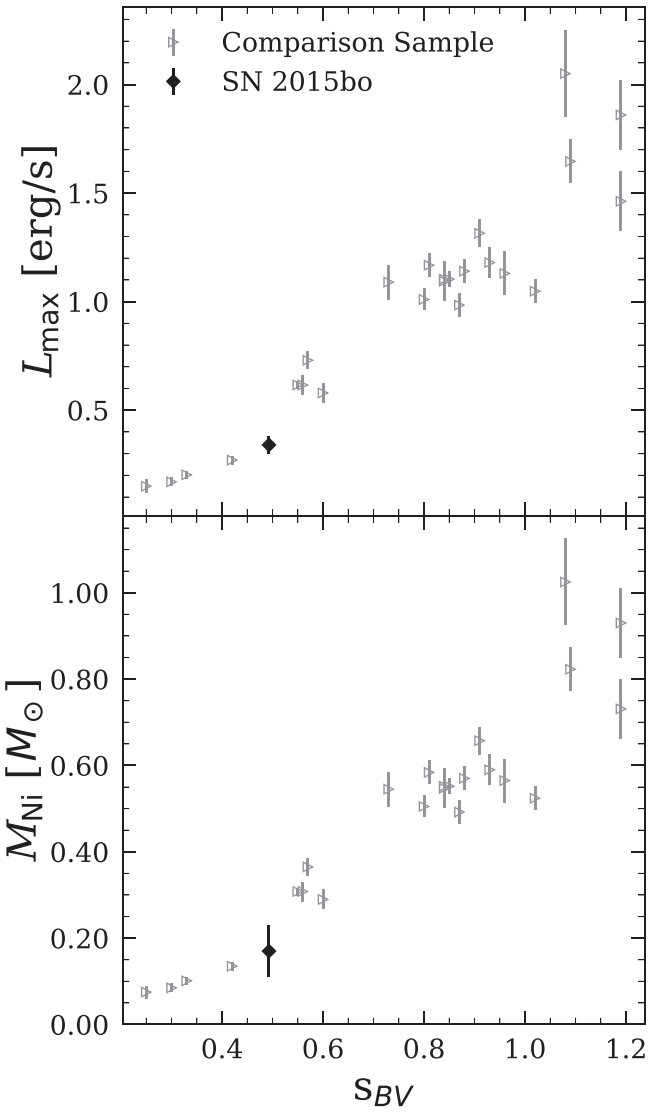

Figure 10. Pseudo-bolometric luminosity (top) and ^{56}Ni mass (bottom) as a function of s_{BV}. SN 2015bo is plotted as the black diamond, while other SNe Ia are hollow, gray right-facing triangles.

are subluminous—strong Si II λ5972 values are predominantly seen in subluminous SNe. SN 2015bo occupies the upper-right area of the Cool region among other fast-declining, subluminous SNe Ia, whereas SN 1997cn falls in the upper-central area of the Cool region.

4.3.2. Velocities

Expansion velocities for each strong spectral feature present in the spectra of SN 2015bo are shown in Figure 15 along with velocities from other SNe Ia for comparison. There are four subluminous SNe (SN 1991bg, SN 1999by, SN 2005bl, and SN 2005ke) and two normal SNe (SN 2011fe and SN 2014J). Comparison velocities are taken from Galbany et al. (2019), and shaded regions represent the Cool and Broad Line regions from Folatelli et al. (2013). Uncertainties are derived from both the uncertainty in the measurement of the minimum of the feature and the resolution limit of the respective instrument used to observe each spectrum. These two uncertainties are added in quadrature to derive the final uncertainty.

For the Ca II H&K feature, SN 2015bo starts at $\sim$18,000 km s^{-1} $\sim$+8 days before $t(B)$max near the normal SNe and decreases over time to reach $\sim$13,000 km s^{-1} at $\sim$+31 days after maximum to be among the subluminous SNe. This evolution does not mirror other subluminous SNe Ia in the sample, which have a flatter velocity evolution going from $\sim$13,000 km s^{-1} at early times to $\sim$11,000 km s^{-1} at later times. The evolution occupies the same space as the Cool region after ~-5 days.

At early times, S II W-blue feature's velocity is similar to SN 2005bl and SN 2014J. The velocity evolution follows the Cool and other 1991bg-like SNe. The evolution has an initial velocity of $\sim$11,000 km s^{-1}, similar to SN 2005bl; however, this drops to $\sim$6000 km s^{-1}, which is similar to other subluminous SNe Ia. The S II W-red feature shows analogous behavior: it starts near SN 2005bl and SN 2014J and declines over time to match the other subluminous Ia.

SN 2015bo has the fastest Si II λ5972 feature of the sample at $\sim$13,500 km s^{-1}. This is in the Broad Line region. It then slows down until it is slower than all the other SNe. Unlike the S II W-red feature, which reaches a homogenous value at ~-5 days, the Si II λ 5972 feature continues to decline until it is the lowest-velocity SN in the sample.

At ~-8 days, SN 2015bo starts faster than all other subluminous SNe Ia Si II λ6355 velocities with the exception of SN 2005bl at $\sim$15,000 km s^{-1}. After declining, the velocities are consistent with other fast-declining SNe Ia and are in the Cool region. At $\sim$+31 days, it is slower than any other member of the comparison sample, with a velocity of $\sim$5000 km s^{-1}.

The two features of Si II λ5972 and Si II λ6355 exhibit velocities that diverge downwards from the Cool pathway of Folatelli et al. (2013) between $\sim$0 days to $\sim$+5 days and $\sim$+10 days to $\sim$+20 days past maximum, respectively. These lower velocities also suggest that the base of the silicon is deeper in SN 2015bo than in all other SNe Ia in the sample.

While noticeable residuals in the corrections for the telluric features are not seen in the epochs with calculated O I λ7774 velocities, they still might exert influence on the calculations. This potential influence can be seen in the significant difference between SN 2015bo and the rest of the comparison sample. However, if these measurements are correct and do not suffer from telluric absoption, then SN 2015bo has the fastest velocities of the sample.

Finally, SN 2015bo's Ca II IR velocity is 18,000 km s^{-1} at ~-10 days, the highest velocity in the entire sample. However, it declines rapidly from $\sim$0 day to $\sim$+10 days; SN 2015bo transitions from being the fastest to the slowest in that time period. After $\sim$+10 days, SN 2015bo declines only slightly over the next 20 days to $\sim$8500 km s^{-1} at +31 days after max.

Overall, the velocities are unique in their steep declines. SN 2015bo starts on the higher end of the 1991bg-like SNe and then finishes on the lower end of the 1991bg-like SNe distribution in nearly every panel of Figure 15. Additionally, SN 2015bo primarily resides outside the Cool region. This behavior is unique to SN 2015bo. Along with the different $V-r$ color curve, this behavior gives evidence that SN 2015bo is different than other 1991bg-like objects.

As is seen in the S and Si velocity evolution, SN 2015bo has an extended layer of IMEs. It is extended to both the highest and lowest velocity compared to SNe of the same subtype. The velocity of the IME region may imply that the burning near the surface was efficient, leaving a lack of unburnt material and

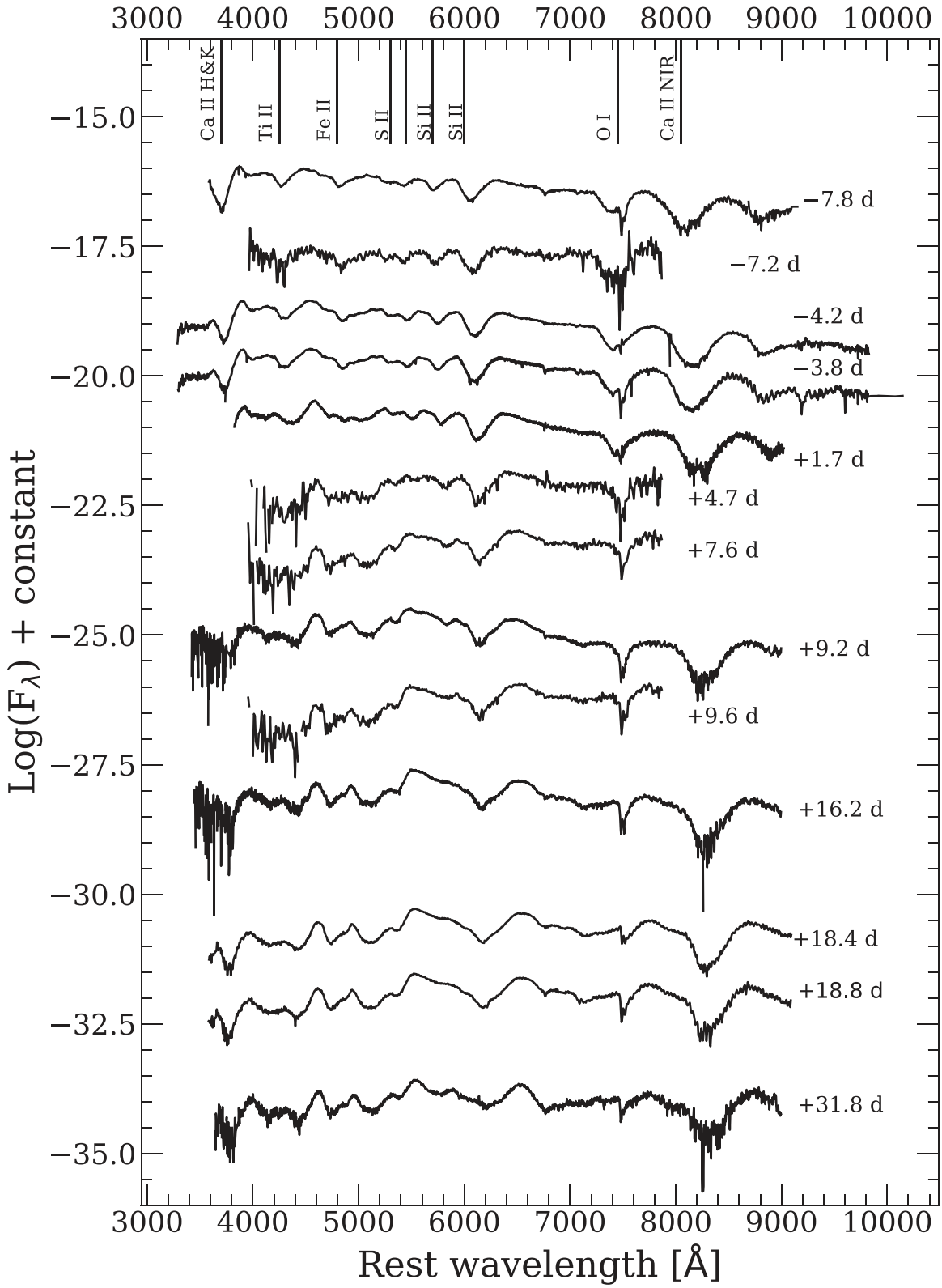

Figure 11. Time series of optical spectra for SN 2015bo. Times relative to $t(B)$max are provided next to each spectrum.
(The data used to create this figure are available.)

producing high-velocity IME lines. Conversely, it also implies that the density of burning in the inner layers (i.e., between 4000–6000 km s^{-1}) was less than about 1×10^7 g cm^{-3}; above this density is where burning to Fe-group elements occur. It is unclear which explosion or progenitor scenarios can produce such a distribution. However, within the framework of a delayed-detonation model the inner region is determined by the transition density (i.e., the density at which the flame front

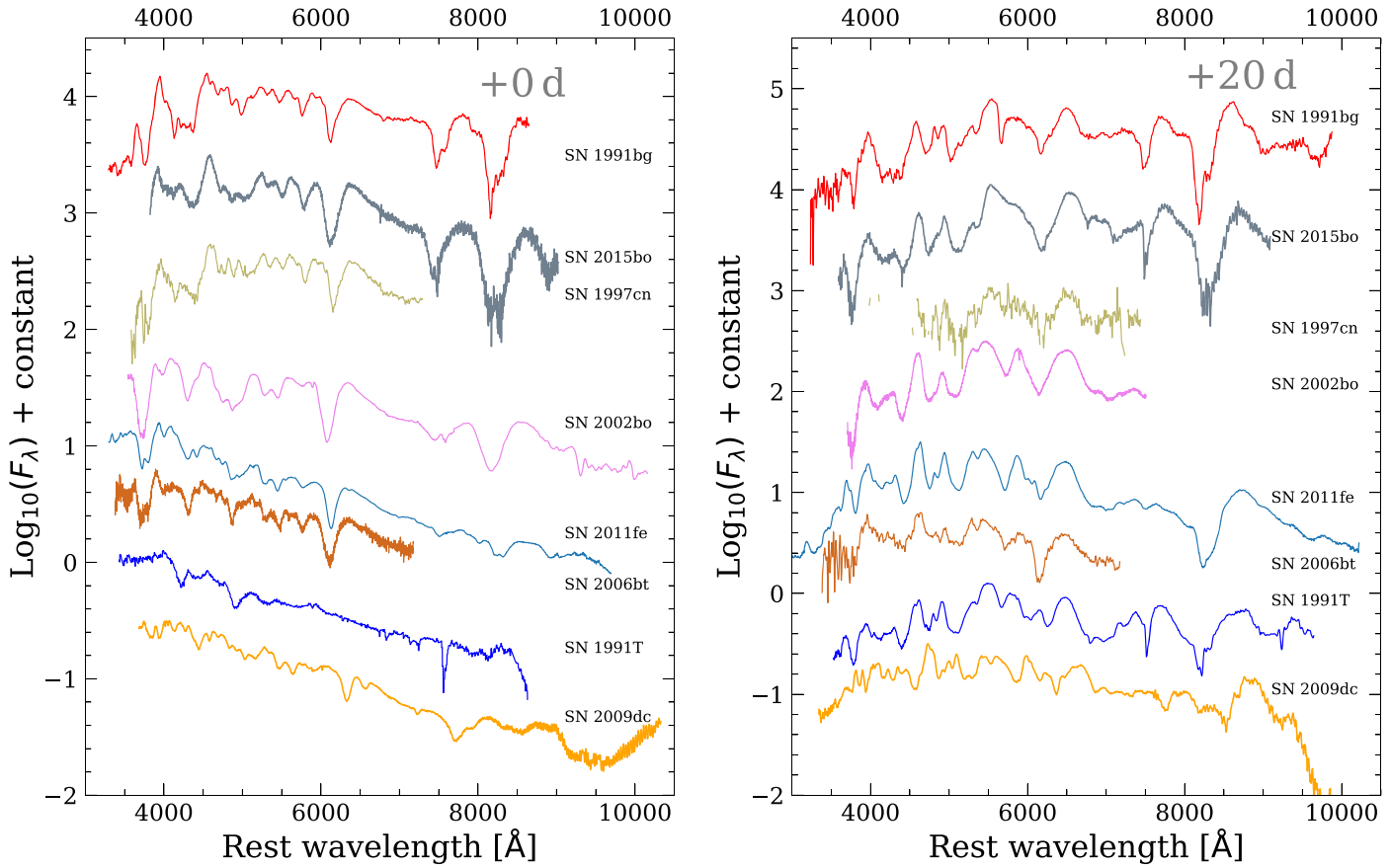

Figure 12. Comparison of SN 2015bo (gray) to other SNe Ia: SN 1991bg (Filippenko et al. 1992b); normal SNe Ia SN 2002bo (Benetti et al. 2004; Szabó et al. 2003) and SN 2011fe (Nugent et al. 2011); peculiar SN 2006bt (Foley et al. 2010); the overluminous SN 1991T (Phillips et al. 1992; Filippenko et al. 1992a); and the 2003fg-like SN 2009dc (Yamanaka et al. 2009). Left: comparison at $t(B)$max. Right: comparison at +20 days from $t(B)$max.

changes from a deflagration to a detonation), and the outer layer is determined by the C–O ratio within the WD (see, e.g., Hoeflich et al. 2017).

4.3.3. Pseudo-equivalent Widths

The pseudo-equivalent widths for SN 2015bo and selected comparison SNe Ia are plotted in Figure 16. The pseudo-equivalent width in Ca II H&K for SN 2015bo is homogenous with the comparison sample even though SN 2015bo starts larger than any other Cool SN, with a value of ∼130 Å. The wavelength coverage of the spectra from ∼0 day to ∼+16 days did not fully capture the feature, so it is uncertain what value SN 2015bo would decline to, if at all. At ∼+31 days after maximum, SN 2015bo has the largest value at ∼115 Å.

In Fe II, SN 2015bo is uniform with the rest of the sample; however, SN 2015bo exhibits a higher maximum value of ∼425 Å at ∼+15 days.

The S II W pseudo-equivalent width deviates from the rest of the sample; it starts near SN 2011fe at ∼75 Å but drops below SN 2014J to ∼60 Å at ∼−5 days. This is followed by a slight increase to ∼70 Å 5 days prior to *B*-band maximum. At ∼+2 days after maximum, SN 2015bo declines down to ∼60 Å. This evolution is not seen in any of the comparison SNe, normal or subluminous. SN 2015bo inhabits the Cool region.

In Si II λ 5972, subluminous SNe have a concave-down morphology and normal SNe have a concave-up morphology. This is an effect of temperature and the heating of the photopshere. Since SN 2015bo is subluminous, it has a concave-down form; it starts at ∼45 Å, which is greater than the rest of the comparison collection, and then increases to a peak of ∼55 Å at ∼+3 days after maximum. From there, SN 2015bo declines slightly to ∼35 Å. The decline for SN 2015bo at ∼+5 days after maximum is earlier than the other subluminous SNe, but this time, perhaps coincidentally, corresponds to the rise of SN 2011fe. SN 2015bo occupies a similar area as the Broad Line region.

SN 2015bo has the same evolution curve as the rest of the sample in Si II λ 6355, however its numerical values are marginally higher. SN 2015bo's maximum m_B time at ∼+20 days after maximum is consistent with the peaks of SN 1991bg and SN 2005bl; however, both SN 1999by and SN 2005ke peak later by ∼10 days. The largest pseudo-equivalent width value of ∼235 Å is larger than the four SNe Ia just mentioned—they peak at ∼180–195 Å. The only SN in the comparison sample that has a higher pseudo-equivalent width is SN 2014J, with a value of ∼255 Å. This value occurs later than SN 2015bo's at ∼+35 days. Beyond ∼+25 days, we expect that the line is blended with Fe II and not just solely Si II emission.

In O I λ 7774, SN 2015bo starts well above the rest of the sample SNe Ia at almost 220 Å ∼−8 days, but it returns to a more consistent value of ∼130 Å at $t(B)$max. The pseudo-equivalent width in O I may suffer from telluric absorption even though only epochs without obvious telluric contamination were selected.

Finally, SN 2015bo starts marginally higher at ∼310 Å at ∼−8 days in Ca II IR, but quickly integrates itself into the mean

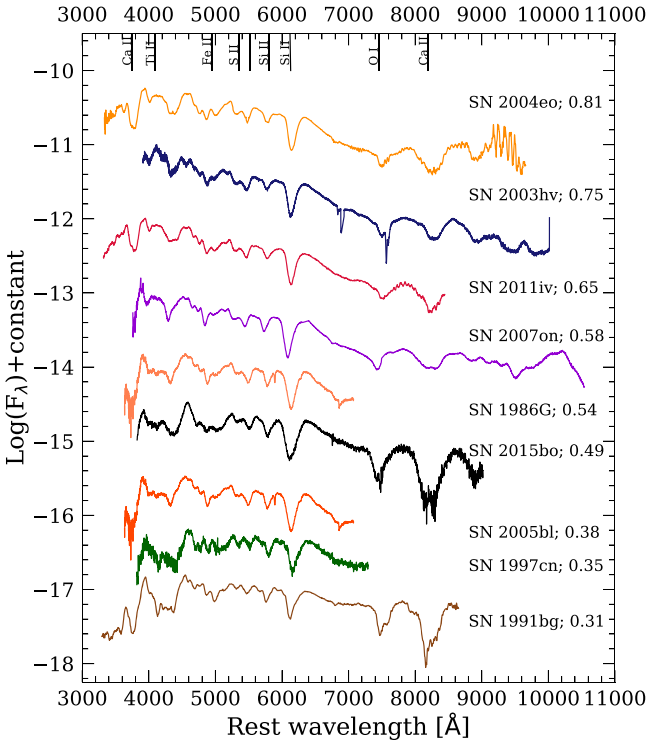

Figure 13. Comparison of optical spectra at $t(B)$max magnitude of 1991bg-like and transitional SNe Ia. From blue to red, the significant features are Ca II H&K $\lambda\lambda$ 3968, 3933, Ti II λ4400, Fe II $\lambda\lambda$ 4923, 5169, S II $\lambda\lambda$ 5449, 5623, Si II $\lambda\lambda$ 5972, 635, O I λ7774, and Ca II $\lambda\lambda$ 8498, 8542, 8662. s_{BV} values are taken from Ashall et al.'s (2018) Table 5, except for SN 1991bg, which is taken from Galbany et al.'s (2019) Table 3.

path of the sample ∼+10 days after maximum at ∼310 Å and rises to reach ∼460 Å at ∼+31 days after maximum.

4.4. Near-infrared Spectrum

The presented NIR spectrum was observed at +11.5 days and is shown in Figure 17. We identify lines of both intermediate-mass and Fe-group elements at this phase. Unlike the optical, NIR spectra reveal different layers of the ejecta at a given epoch (Höflich et al. 2002). Specifically, we identify Ca II $\lambda\lambda$ 8662, 8538, Mg II $\lambda\lambda$ 9227, 10927, Si II λ11737, Ca II $\lambda\lambda$ 11839, 11950, and Fe II features, as well as significant Fe and Co emission between the two telluric bands in the *H*-band break. Finally, strong Co II emission is present in the 2 μm to 2.4 μm region. Eight Co II lines dominate this region: Co II $\lambda\lambda$ 20913, 21211, 21351, 21509, 22209, 22482, 23619, and 24603 (Gall et al. 2012).

There is an area of strong Fe II, Co II, and Ni II emission, known as the *H*-band break, that originates from allowed transitions above the photosphere (Wheeler et al. 1998). Hsiao et al. (2013) found a correlation between the SN stretch parameter and the feature strength of the *H*-band break and that the *H*-band break strength should be near its maximum value at the phase of our observed NIR spectrum. Ashall et al. (2019a, 2019b) showed that this feature can be used to determine the location of the outermost ^{56}Ni in SNe Ia using the v_{edge} parameter. The v_{edge} parameter is the velocity of the bluest edge of the *H*-band break Co II emission line; see Ashall et al. (2019a) for further details. v_{edge} is plotted against s_{BV} in Figure 18 using data from Ashall et al. (2019a).

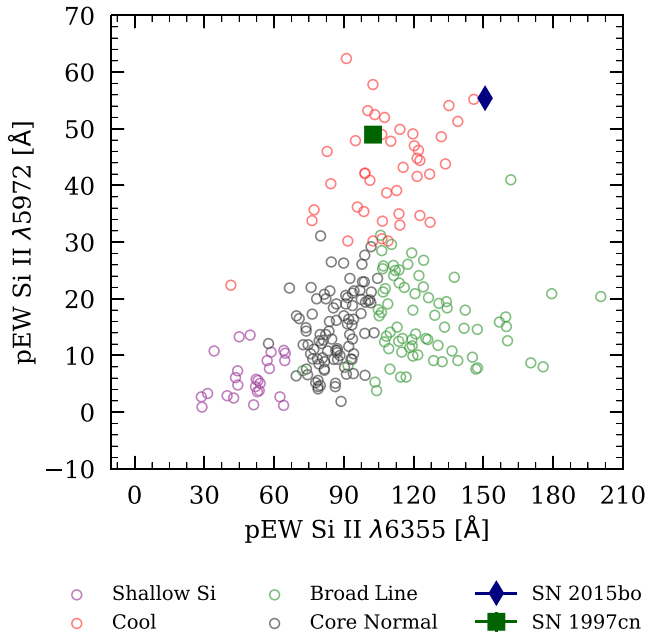

Figure 14. Branch diagram (Branch et al. 2006) with SN 2015bo as the blue diamond and SN 1997cn as the dark green square. Data for other SNe Ia are from Blondin et al. (2012) and Folatelli et al. (2013).

Table 3
Log of Spectroscopic Observations

UT Data	MJD (days)	Epoch[a] (days)	Telescope	Spectrograph
2015-02-15	57068.35	−7.8	NTT[b]	EFOSC2
2015-02-16	57069.00	−7.2	LT[c]	SPRAT
2015-02-19	57072.00	−4.2	LT	SPRAT
2015-02-19	57072.34	−3.9	NTT	EFOSC2
2015-02-19	57072.36	−3.9	NTT	EFOSC2
2015-02-25	57078.00	1.7	DUP[d]	WFCCD
2015-02-28	57081.00	4.7	LT	SPRAT
2015-03-03	57084.00	7.6	LT	SPRAT
2015-03-03	57085.64	9.2	NOT[e]	ALFOSC
2015-03-05	57086.00	9.6	LT	SPRAT
2015-03-07	57088.00	11.5	Magellan	FIRE
2015-03-10	57092.69	16.2	NOT	ALFOSC
2015-03-14	57095.00	18.4	LT	SPRAT
2015-03-14	57095.30	18.7	NTT	EFOSC2
2015-03-14	57095.32	18.8	NTT	EFOSC2
2015-03-26	57108.63	31.8	NOT	ALFOSC

Notes.
[a] Epoch phase relative to rest-frame *B*-band maximum.
[b] New Technology Telescope.
[c] Liverpool Telescope.
[d] du Pont Telescope.
[e] Nordic Optical Telescope.

SN 2015bo's v_{edge} is -7000 ± 1300 km s^{-1} (Ashall et al. 2019b). This shows that the majority of the ^{56}Ni mass is located in the center of the ejecta. This also implies a low ^{56}Ni mass, as found in Section 3.4.

5. Distance to NGC 5490 and 1991bg-like Supernovae as Distance Indicators

SN 2015bo has a sibling (a SN in the same host galaxy): SN 1997cn (Li et al. 1997; Turatto et al. 1998; Jha et al. 2006).

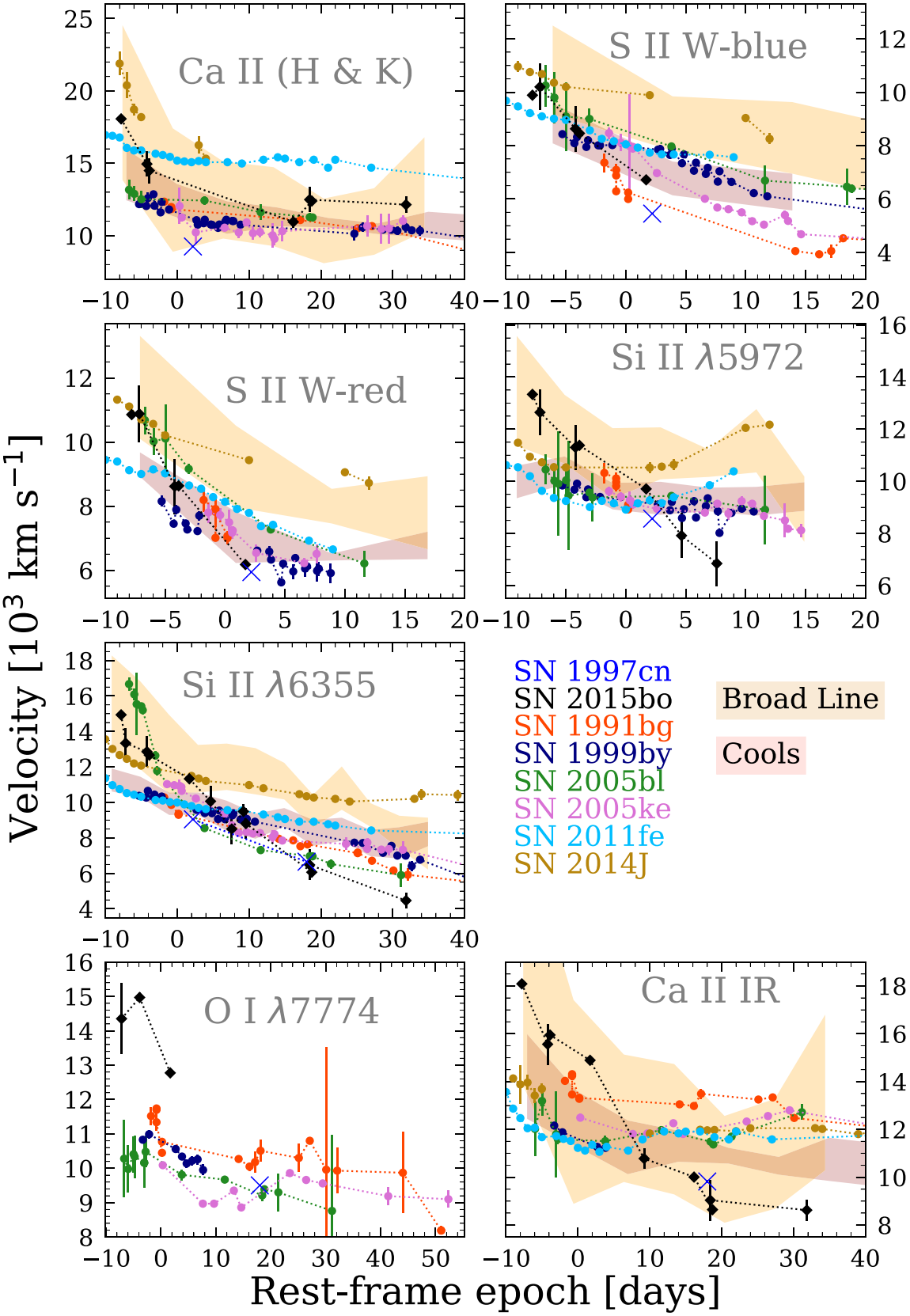

Figure 15. Velocities of SN 1997cn (blue X), SN 2015bo (black diamonds) and other SNe Ia (other colors, circles). The tan and salmon shaded areas are the 1σ dispersion regions of the Broad Line and Cool evolutionary paths presented in Folatelli et al. (2013) using CSP-I data.

Interestingly, SN 2015bo and SN 1997cn are also both fast decliners, so not only are they siblings, they are also of the same spectral subtype (nominally called "twins"). Since fast decliners are located preferentially in early-type galaxies (Hamuy et al. 1996), it is unsurprising that an early-type galaxy is the host of two fast-declining SNe, as opposed to a

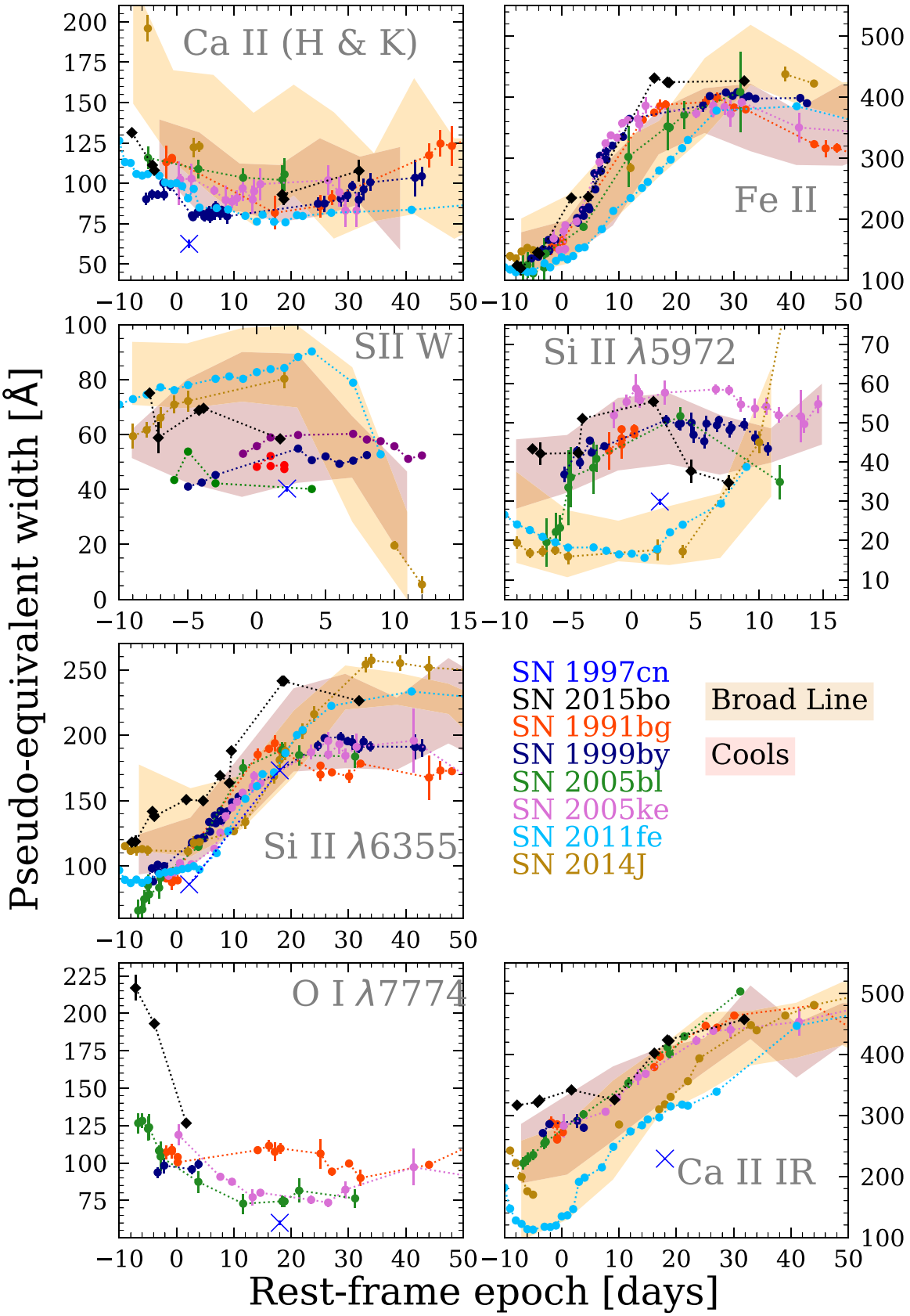

Figure 16. Pseudo-equivalent widths of SN 1997cn (blue X) SN 2015bo (black diamonds) and other SNe Ia (other colors, circles). The tan and salmon shaded areas are the 1σ dispersion regions of the Broad Line and Cool evolutionary paths presented in Folatelli et al. (2013) using CSP-I data.

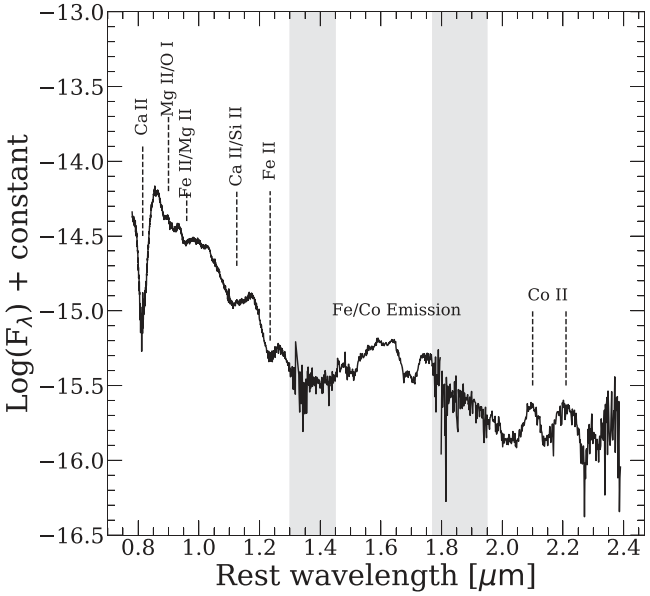

Figure 17. NIR spectrum of SN 2015bo at +11.5 days. Telluric regions are denoted by gray bands. Spectral features are labeled on the plot and described in the text.

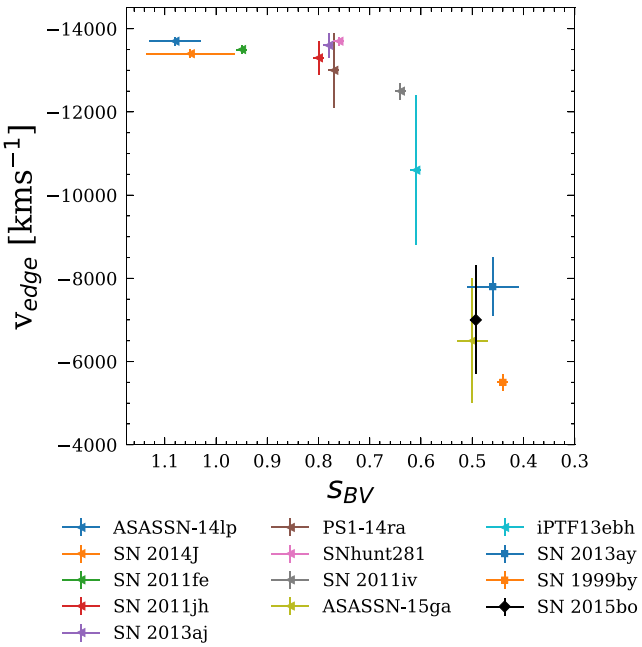

Figure 18. $v_{\rm edge}$ vs. $s_{\rm BV}$ plot using data from Ashall et al. (2019b). $v_{\rm edge}$ is the velocity of the bluest Co II emission line in the *H*-band break. SN 2015bo is plotted as the black diamond in the bottom right.

different galaxy type where fast-declining SNe Ia are even less common. This provides an opportunity to evaluate the accuracy and consistency of these quasi-rare subtypes as distance indicators. To date, this is the only known instance of two fast-declining SNe exploding in the same host galaxy. In this section, distance moduli are derived using various methods and checked for consistency.

We calculate the distance modulus to the host (NGC 5490) with three independent methods: (i) the $z_{\rm cmb}$ distance-derived method assuming a cosmology of $H_0 = 73\,{\rm km\,s^{-1}\,Mpc^{-1}}$, $\Omega_m = 0.27$, and $\Omega_\Lambda = 0.73$; (ii) the independent distance derived using the photometry of all available bands of SN 2015bo; and (iii) the independent distance derived using the photometry of all available bands of SN 1997cn. All of the derived distances, as well as the distance computed using surface-brightness fluctuations (Jensen et al. 2021), can be found in Table 4.

Table 4
Distance Moduli Derived Using Four Independent Methods: $z_{\rm cmb}$ Cosmology, Surface-brightness Fluctuations, SN 2015bo, and SN 1997cn

Object	μ (mag)	σ_μ (mag)
NGC 5490[a]	34.21	0.15
NGC 5490[b]	34.27	0.08
SN 2015bo	34.33	0.01 (stat) 0.11 (sys)
SN 1997cn	34.34	0.04 (stat) 0.12 (sys)

Notes.
[a] Corrected to the cosmic microwave background rest frame and calculated using $H_0 = 73\,{\rm km\,s^{-1}\,Mpc^{-1}}$, $\Omega_m = 0.27$, and $\Omega_\Lambda = 0.73$, which is used throughout this work.
[b] Distance derived from surface-brightness fluctuation distance from Jensen et al. (2021).

The distance modulus derived using the $z_{\rm cmb}$ method is $\mu = 34.21 \pm 0.15$ mag. As discussed in Section 3.1, the distance modulus to SN 2015bo was determined using the EBV2 model and a 1991bg-like *K*-correction in SNooPy with the prior that $E(B-V)_{\rm Host} = 0$ in the fit. Photometry for SN 2015bo is in the CSP natural system. SNooPy has an uncertainty budget described in Burns et al. (2011). Of the four categories, only the uncertainty from the stretch parameter applies to SN 2015bo. To compute the systematic uncertainty for $s_{\rm BV}$, the dispersion in the fit between $s_{\rm BV}$ and $\Delta{\rm m15}(B)$ is considered. Because these are independent measures of the decline rate, the source of the dispersion in this relation comes from both random noise (due to measurement error) and any systematic errors that $s_{\rm BV}$ and $\Delta{\rm m15}(B)$ have in measuring the "true" decline rate. Therefore the dispersion is an upper limit on the systematic error in $s_{\rm BV}$ (or $\Delta{\rm m15}(B)$). This value is $\sigma s_{\rm BV} = 0.03$, which turns into an uncertainty in distance modulus of ± 0.11 mag. Thus, we calculate a distance modulus of $\mu = 34.33 \pm 0.01\,({\rm stat}) \pm 0.11\,({\rm sys})$ mag.

The standard system filters are used when fitting the photometry of SN 1997cn with SNooPy because the data for SN 1997cn is in the standard system. Since there is not enough photometric data to accurately determine $t(B)$max, the best spectrum for SN 1997cn was used as input in SuperNovae IDentification (SNID) to determine the time of maximum using the spectrum. The best SNID match was to the 1991bg-like SN 1998de (Modjaz et al. 2001) at +2.7 days old. The time from this match ($t(B)$max = 50587.8 MJD) was then given to SNooPy to use as the time of the *B*-band maximum. Without constraining $t(B)$max, SNooPy struggles to reasonably fit the light curves. This is because SNooPy seeks to fit the *I* band with two maxima-like normal SNe Ia; however, SN 1997cn does not have a second maximum. This causes the fit to be poor, so the fit is given the $t(B)$max from SNID as a prior. We also choose to leave host-galaxy extinction as a free parameter for SN 1997cn. Apart from these differences, the fitting methods used to derive the distance modulus of SN 1997cn are the same as the ones used to derive the distance modulus of SN 2015bo. Only the data from Jha et al. (2006) was used

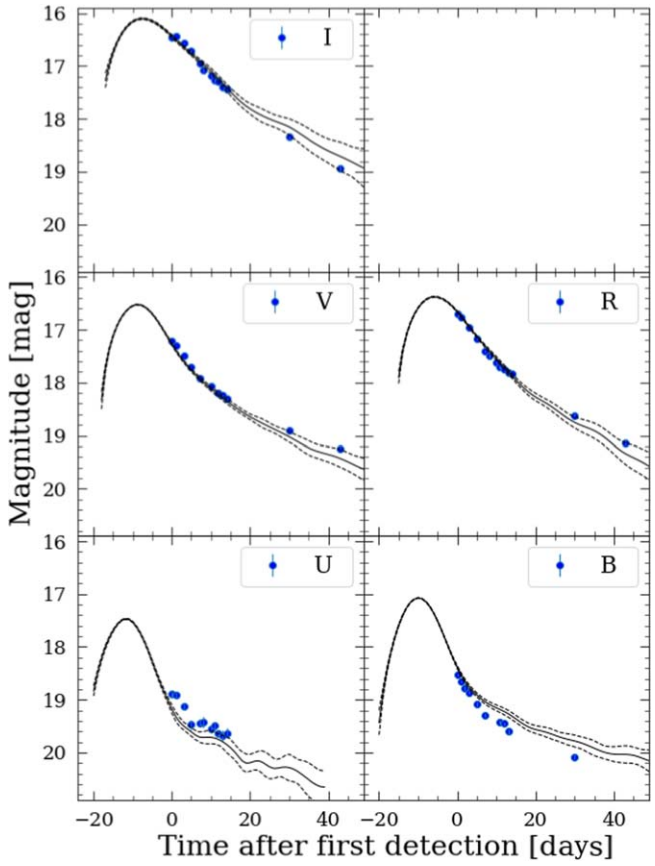

Figure 19. SNooPy fits for SN 1997cn. Data from Jha et al. (2006). The fits are constrained by using the $t(B)$max from SNID. Host-galaxy extinction is a free parameter for these fits.

because it was obtained on a single telescope and published in the standard system. Turatto et al. (1998) used data from multiple telescopes and it is unclear what system the data is in. Fits for SN 1997cn are presented in Figure 19.

To calculate the total SNooPy systematic uncertainty in SN 1997cn, we must consider the systematic uncertainty from reddening in addition to the intrinsic spread in $s_{\rm BV}$. The reddening uncertainty was determined via two methods. The first method took the systematic uncertainty as the difference between distance modulus when calculated with $E(B-V)_{\rm Host}$ as a free parameter and held fixed to a value of 0. This gave a systematic uncertainty in distance modulus of ± 0.01 mag for SN 1997cn. The second method was to use the intrinsic dispersion in the B-V intrinsic color. The dispersion is ± 0.06, so one could also simply adopt that as a systematic. This gives an uncertainty of ± 0.04 mag for SN 1997cn. The method with the larger value was chosen to be used in the final analysis and was added in quadrature with the $s_{\rm BV}$ systematic uncertainty to arrive at a final distance modulus of $\mu = 34.34 \pm 0.04\,({\rm stat}) \pm 0.12\,({\rm sys})$ mag.

Adding the statistical and systematic errors in quadrature for SN 1997cn and SN 2015bo gives values of $\mu_{97\,{\rm cn}} = 34.34 \pm 0.13$ mag and $\mu_{15{\rm bo}} = 34.33 \pm 0.11$ mag. The difference in distance modulus is $\Delta\mu = 0.01 \pm 0.17$ mag, again with the errors added in quadrature. The distances differ by less than 0.06σ.

Figure 20 provides a visual representation of the distance moduli where the consistency is clearly seen, in addition to

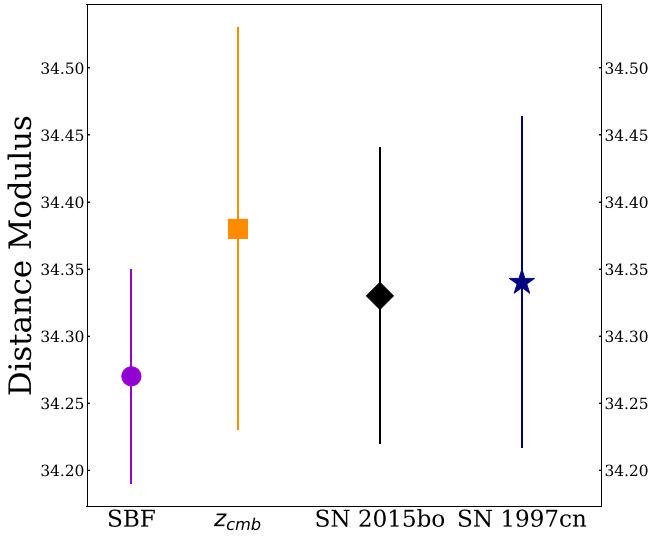

Figure 20. Graphical comparison of distance moduli derived from surface-brightness fluctuation (SBF; taken from Jensen et al. 2021), $z_{\rm cmb}$-corrected cosmology, SN 2015bo, and SN 1997cn. All values are consistent with each other.

distance moduli from both redshift-corrected cosmology and surface-brightness fluctuations from Jensen et al. (2021). Note that there is most likely further uncertainty due to the fits for SN 1997cn being poorly constrained from the lack of data prior to maximum in all bands. This will add in an extra uncertainty in the value for SN 1997cn. Therefore, the presented values are lower bounds for the uncertainty. Considering this, it appears that fast decliners might be equally standardizable as normal SNe Ia and could offer the same robust functionality. The result from Burns et al. (2018) supports this hypothesis: they found SN 2006mr to be consistent with the three other SNe Ia in Fornax A (Stritzinger et al. 2010).

However, there have been inconsistencies in the past with using twins and siblings when deriving distances. Foley et al. (2020) found a significant ($\delta {\rm M}_V = 0.335 \pm 0.069$ mag) difference between the peak V-band magnitudes of 2011by and 2011fe, but these SNe were hosted by different galaxies—NGC 3972 and M101, respectively—and they may be influenced by peculiar velocities. Gall et al. (2018) found that two transitional SNe (SN 2007on and SN 2011iv) that exploded in the same host galaxy produce a statistical difference in calculated distance moduli in both B and H bands, finding the two objects' distance moduli differed by $\sim$14% and $\sim$9% in the B and H bands, respectively. On the other hand, SN 2015bo and SN 1997cn are in the same host galaxy, have similar spectra, and have consistent distances. This tension can be resolved with further twin studies of fast decliners.

The maximum light spectral similarity of SN 1997cn and SN 2015bo can be seen in Figure 21. The "twinness" parameter described by Fakhouri et al. (2015) was calculated to be 1.04, which puts it in the median range of twinness. This parameter is akin to a reduced χ^2 parameter, and therefore it is sensitive to estimated errors. This estimated error dominates the spectra, possibly due to the data being taken on different telescopes and instruments, and thus the twinness parameter may not be the best indicator of how alike two spectra or SNe Ia are unless the quality of the input data is similar.

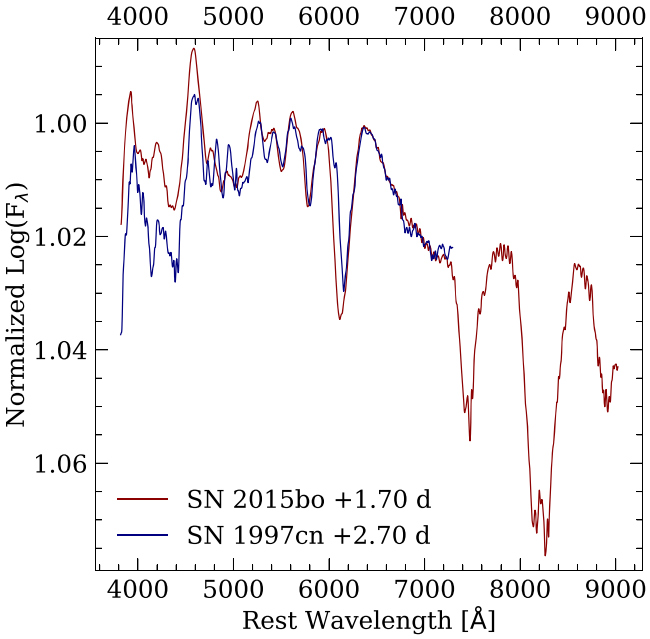

Figure 21. Comparison of the spectra of SN 1997cn (navy) and SN 2015bo (dark red). The spectra have been color-corrected to match the photometric measurements, put through a Gaussian 3σ smoothing function, and were normalized to the blue edge of the Si II λ 6355 feature.

6. Conclusion

Photometric *uBVgriYHJ* data of SN 2015bo from −2.9 days to +103.8 days and spectroscopic data from −7.8 days to 31.8 days from maximum light are presented. Tables B1 and B2 contain logs of the optical and NIR photometric observations. SN 2015bo is a fast-declining, underluminous SN Ia that exploded in NGC 5490. SN 2015bo has an absolute magnitude $M_B = -17.50 \pm 0.15$ mag. It has $\Delta m15(B) = 1.91 \pm 0.01$ (mag) and $s_{\rm BV} = 0.48 \pm 0.01$.

Photometrically, SN 2015bo is subluminous and fast declining, and it occupies the same parameter space as other underluminous fast decliners in the luminosity–width relation. This is confirmed in the $s_{\rm BV}$ versus $t_{\rm max}^{i-B}$ diagram, where SN 2015bo is positioned among 1991bg-like SNe. The light curves evolve quickly, and SN 2015bo has unique morphologies in the $V-r$ and $r-i$ color curves. In the $V-r$ color curve, it is the bluest SNe in the plotted sample even with extinction corrections applied. In the $r-i$ color curve, it displays a redward climb at ∼+40 days. This may be a way to identify peculiar subluminous SNe in future surveys. SN 2015bo has a peak bolometric luminosity of $L_{\rm bolo}^{\rm peak} = 0.33 \pm 0.03 \times 10^{43}$ erg s^{-1}, which corresponds to a nickel mass of $0.17 \pm 0.05\ M_\odot$. This value may change slightly if the full Arnett's rule and a rise time were used.

Spectroscopically, SN 2015bo shows the standard features typical for a fast decliner. In the Branch et al. (2006) diagram, SN 2015bo resides among other Cool SNe Ia. SN 2015bo's velocities range from ∼18,000 km s^{-1} to ∼4000 km s^{-1} and decrease over time.

Importantly, SN 2015bo exploded in the same host galaxy as SN 1997cn, another fast decliner. Distances to both SN 2015bo and SN 1997cn were calculated and are consistent with each other at the 0.06σ level. We suggest that fast decliners are consistent and standardizable, and hence they should *not* be omitted from future cosmological work. A future study of two or more fast-declining siblings with two or more well-sampled objects will offer a chance to confirm this result.

We thank the anonymous referee for their comments. W.B. H. acknowledges support from the Research Experience for Undergraduates program at the Institute for Astronomy, University of Hawaii-Manoa, funded through NSF grant #2050710. L.G. acknowledges financial support from the Spanish Ministry of Science, Innovation and Universities (MCIN) under the 2019 Ramón y Cajal program RYC2019-027683 and from the Spanish MCIN project HOSTFLOWS PID2020-115253GA-I00. M.G.M., R.G.D., and S.M.T. were funded by the European Union's Horizon 2020 research and innovation program under the Marie Skłodowska-Curie grant agreement No. 839090. Based on observations collected at the European Southern Observatory under ESO program 106.2104. The work of the CSP-II has been generously supported by the National Science Foundation under grant Nos. AST-1008343, AST-1613426, AST-1613455, and AST-1613472. The CSP-II was also supported in part by the Danish Agency for Science and Technology and Innovation through a Sapere Aude Level 2 grant. E.B. was partially supported by NASA grant No. 80NSSC20K0538 J.D.L. acknowledges support from a UK Research and Innovation Fellowship (MR/T020784/1). C.R. B. acknowledges support from NSF grant Nos. AST-1008384, AST-1613426, AST-1613455, and AST-1613472.

M.S and S.H. are supported by grants from the VILLUM FONDEN (grant No. 28021) and the Independent Research Fund Denmark (IRFD; 8021-00170B).

Appendix A
SN 1997cn Light Curves

Light curves for SN 1997cn are presented in Figure A1, as well as $t(B)$max as derived from SNooPy, SNID spectrum analysis, and the spectral modeling performed by Turatto et al. (1998). Turatto et al. (1998) estimate B-band maximum occurred on 1997 May 19 (2450587.50 JD), which is +18 days after the inferred explosion. The time derived by SNooPy using data from Jha et al. (2006) is 2450580.72 ± 0.70 JD. The difference is $\Delta t(B)\text{max} = 6.78$ days. The SNooPy $t(B)$max is before the discovery point; however, the discovery point could be close to maximum. Given that the data was taken without a filter, it most likely resembles V- or R-band photometry. The SNID $t(B)$max is 2450588.3 JD. This time yields the best SNooPy fits of the light curves. SNooPy differs from these dates because there is no well-defined maximum in the light curves for SN 1997cn. The exact date of maximum is uncertain. This comes from the fact that comprehensive, all-sky surveys for SNe were not available when SN 1997cn exploded.

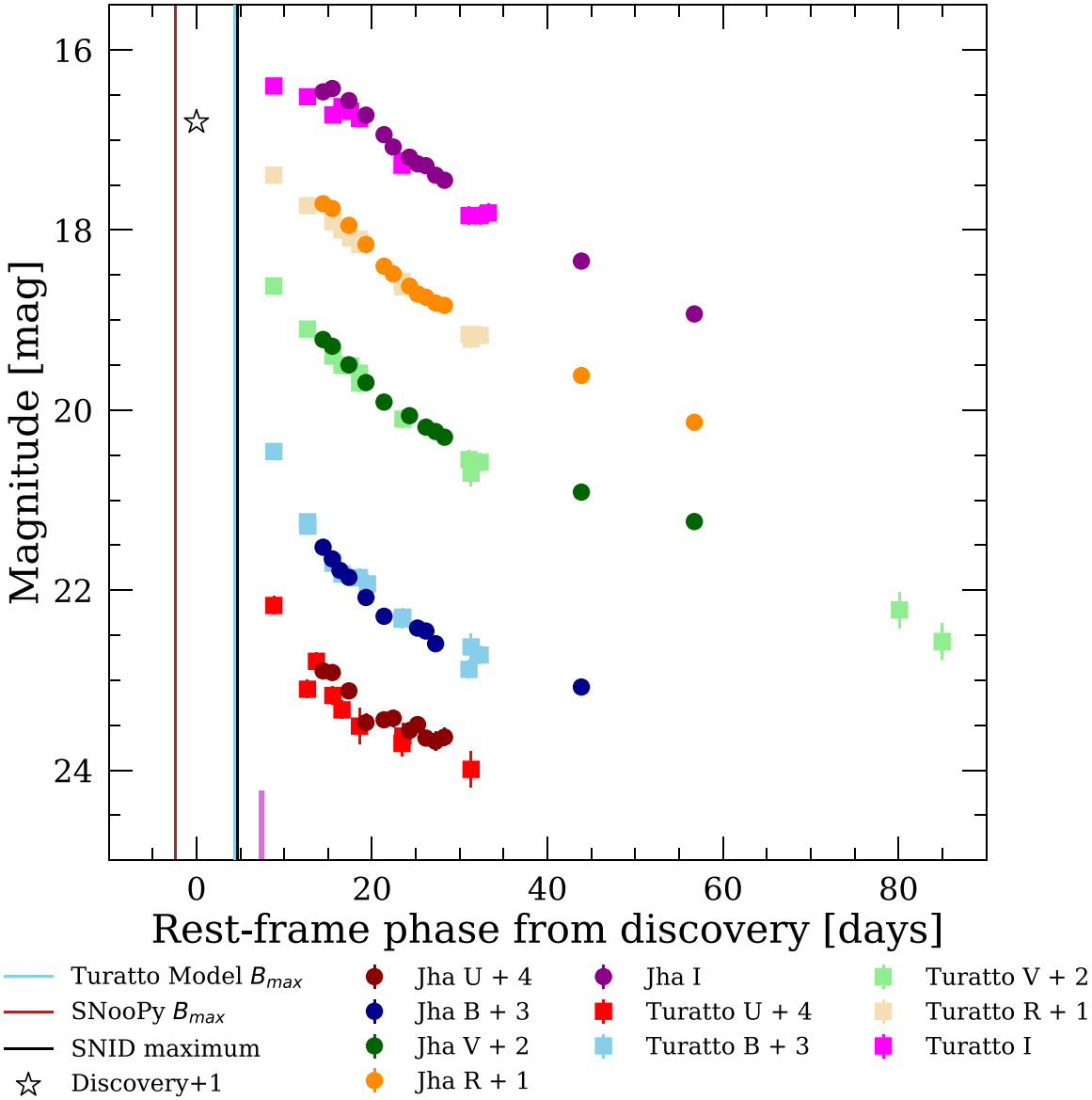

Figure A1. Light curves of SN 1997cn. The discovery datum point is from Li et al. (1997) and is denoted by a hollow black star; lightly filled, square data points are from Turatto et al. (1998), and darkly filled, circle data points are from Jha et al. (2006). The discovery point from Li et al. (1997) uses an unfiltered CCD exposure. This point is plotted as if it was in the *R* band. The magenta line represents the date of the earliest spectrum for SN 1997cn.

Appendix B
Photometric Data

Table B1
Log of Optical Photometric Data

day (MJD)	u (mag)	B (mag)	V (mag)	g (mag)	r (mag)	i (mag)
57069.4	18.51(0.03)	17.49(0.01)	17.30(0.01)	17.35(0.01)	17.21(0.01)	17.49(0.01)
57075.4	18.16(0.02)	16.84(0.01)	16.52(0.01)	16.63(0.01)	16.37(0.01)	16.66(0.01)
57076.3	18.24(0.02)	16.86(0.01)	16.47(0.01)	16.63(0.01)	16.32(0.01)	16.65(0.01)
57079.4	18.55(0.03)	17.08(0.01)	16.48(0.01)	16.76(0.01)	16.28(0.01)	16.64(0.01)
57080.3	18.66(0.03)	17.22(0.01)	16.51(0.01)	16.86(0.01)	16.30(0.01)	16.65(0.01)
57082.3	…	17.55(0.01)	16.66(0.01)	17.13(0.01)	…	…
57082.4	19.07(0.03)	…	…	…	16.37(0.01)	16.72(0.01)
57083.3	19.22(0.04)	17.71(0.01)	16.74(0.01)	17.28(0.01)	16.44(0.01)	16.75(0.01)
57084.3	19.41(0.05)	17.90(0.02)	16.84(0.01)	17.46(0.02)	16.50(0.01)	16.79(0.02)
57085.3	19.62(0.06)	18.05(0.02)	16.96(0.02)	17.59(0.02)	16.56(0.01)	16.78(0.01)
57086.3	…	…	17.10(0.02)	17.76(0.02)	16.65(0.01)	16.83(0.01)
57086.4	…	18.15(0.02)	…	…	…	…
57087.3	…	18.32(0.03)	17.16(0.01)	17.93(0.02)	16.71(0.01)	16.83(0.01)
57087.4	19.76(0.15)	…	…	…	…	…
57088.3	…	18.45(0.02)	17.27(0.02)	18.02(0.02)	16.77(0.01)	16.86(0.02)
57089.3	…	18.59(0.03)	17.37(0.02)	18.18(0.02)	16.85(0.01)	16.88(0.01)
57090.4	…	18.70(0.03)	17.45(0.02)	18.27(0.02)	16.92(0.01)	16.93(0.01)
57091.3	…	18.79(0.02)	17.56(0.01)	18.36(0.02)	16.99(0.01)	16.97(0.01)
57092.4	…	18.83(0.03)	17.65(0.02)	18.42(0.02)	17.06(0.01)	17.04(0.01)
57093.3	…	19.00(0.02)	17.70(0.01)	18.54(0.02)	17.16(0.01)	17.10(0.01)
57094.3	…	19.01(0.02)	17.82(0.02)	…	…	…
57094.4	…	…	…	18.62(0.02)	17.23(0.01)	17.17(0.01)
57095.3	…	19.08(0.02)	17.88(0.01)	18.68(0.02)	…	…
57095.4	…	…	…	…	17.32(0.01)	17.24(0.01)
57096.3	…	19.14(0.02)	17.97(0.02)	…	…	…
57096.4	…	…	…	18.75(0.02)	17.42(0.01)	17.32(0.01)
57097.3	…	…	…	18.83(0.02)	17.52(0.01)	…
57097.4	…	19.24(0.02)	18.04(0.02)	…	…	17.44(0.01)
57098.3	…	…	…	18.88(0.02)	17.62(0.01)	17.54(0.01)
57098.4	…	19.25(0.02)	18.14(0.02)	…	…	…
57099.3	…	19.32(0.02)	18.20(0.02)	18.89(0.02)	17.70(0.01)	17.62(0.01)
57100.3	…	19.39(0.02)	18.27(0.02)	19.00(0.02)	17.79(0.01)	17.71(0.01)
57101.3	…	19.46(0.02)	18.33(0.01)	19.04(0.02)	17.84(0.01)	17.79(0.01)
57102.3	…	19.49(0.02)	18.38(0.02)	19.11(0.02)	17.89(0.01)	17.84(0.02)
57103.4	…	…	18.42(0.04)	19.13(0.04)	17.81(0.06)	…
57104.3	…	…	…	…	18.00(0.02)	…
57109.3	…	…	…	…	18.23(0.01)	…
57109.4	…	19.67(0.02)	18.62(0.02)	19.27(0.02)	…	18.24(0.02)
57110.2	…	…	…	19.34(0.02)	18.29(0.01)	…
57110.3	…	19.69(0.02)	18.68(0.02)	…	…	18.30(0.02)
57111.3	…	19.76(0.02)	18.71(0.02)	19.36(0.02)	18.33(0.01)	18.39(0.02)
57112.3	…	19.66(0.02)	18.73(0.02)	19.37(0.02)	18.38(0.01)	18.39(0.01)
57113.3	…	19.74(0.05)	18.77(0.02)	19.37(0.04)	18.42(0.02)	18.47(0.02)
57117.2	…	…	…	19.40(0.06)	18.58(0.03)	…
57117.3	…	19.76(0.09)	18.91(0.05)	19.45(0.06)	…	18.64(0.03)
57119.3	…	19.76(0.07)	18.96(0.04)	…	18.64(0.02)	18.73(0.03)
57121.2	…	19.92(0.04)	19.00(0.02)	19.54(0.03)	18.72(0.02)	18.79(0.02)
57123.3	…	20.00(0.04)	19.05(0.02)	19.55(0.02)	18.82(0.02)	18.88(0.02)
57126.2	…	20.03(0.02)	19.17(0.02)	…	…	…
57126.3	…	…	…	19.64(0.02)	18.98(0.02)	19.04(0.02)
57129.2	…	20.05(0.02)	19.26(0.02)	19.67(0.02)	19.08(0.02)	19.16(0.02)
57131.3	…	20.07(0.02)	19.32(0.02)	19.70(0.02)	19.15(0.02)	19.21(0.02)
57134.3	…	20.10(0.03)	19.38(0.02)	19.77(0.02)	19.30(0.02)	19.30(0.03)
57136.3	…	20.13(0.03)	19.42(0.02)	19.81(0.02)	19.35(0.02)	19.40(0.03)
57138.2	…	20.16(0.03)	19.50(0.02)	19.84(0.02)	19.42(0.02)	19.45(0.02)
57153.2	…	20.43(0.04)	19.85(0.03)	20.10(0.03)	20.05(0.03)	19.94(0.05)
57160.2	…	20.61(0.04)	20.04(0.03)	20.18(0.03)	20.26(0.04)	20.15(0.07)
57180.1	…	…	…	20.61(0.04)	20.98(0.07)	…
57181.2	…	…	…	20.50(0.09)	…	…
57182.1	…	…	20.38(0.09)	20.60(0.07)	…	…

Note.

(This table is available in machine-readable form.)

Table B2
Log of Near-infrared Photometric Data

day (MJD)	J (mag)	H (mag)	Y (mag)
57088.3	16.97(0.02)	16.51(0.02)	16.30(0.01)
57089.4	16.97(0.03)	16.53(0.02)	16.31(0.01)
57090.4	17.00(0.03)	16.59(0.02)	16.31(0.01)
57091.3	17.06(0.03)	16.57(0.02)	16.32(0.01)
57093.3	17.15(0.02)	16.72(0.02)	16.35(0.01)

ORCID iDs

W. B. Hoogendam https://orcid.org/0000-0003-3953-9532
C. Ashall https://orcid.org/0000-0002-5221-7557
L. Galbany https://orcid.org/0000-0002-1296-6887
B. J. Shappee https://orcid.org/0000-0003-4631-1149
C. R. Burns https://orcid.org/0000-0003-4625-6629
J. Lu https://orcid.org/0000-0002-3900-1452
M. M. Phillips https://orcid.org/0000-0003-2734-0796
E. Baron https://orcid.org/0000-0001-5393-1608
S. Holmbo https://orcid.org/0000-0002-3415-322X
E. Y. Hsiao https://orcid.org/0000-0003-1039-2928
N. Morrell https://orcid.org/0000-0003-2535-3091
M. D. Stritzinger https://orcid.org/0000-0002-5571-1833
N. B. Suntzeff https://orcid.org/0000-0002-8102-181X
F. Taddia https://orcid.org/0000-0002-2387-6801
D. R. Young https://orcid.org/0000-0002-1229-2499
J. D. Lyman https://orcid.org/0000-0002-3464-0642
S. Benetti https://orcid.org/0000-0002-3256-0016
P. A. Mazzali https://orcid.org/0000-0001-6876-8284

References

Adelman-McCarthy, J. K., Agüeros, M. A., Allam, S. S., et al. 2008, ApJS, 175, 297
Arnett, W. D. 1982, ApJ, 253, 785
Ashall, C., Hoeflich, P., Hsiao, E. Y., et al. 2019b, ApJ, 878, 86
Ashall, C., Hsiao, E. Y., Hoeflich, P., et al. 2019a, ApJL, 875, L14
Ashall, C., Lu, J., Burns, C., et al. 2020, ApJL, 895, L3
Ashall, C., Lu, J., Hsiao, E. Y., et al. 2021, ApJ, 922, 205
Ashall, C., Mazzali, P. A., Pian, E., & James, P. A. 2016, MNRAS, 463, 1891
Ashall, C., Mazzali, P. A., Stritzinger, M. D., et al. 2018, MNRAS, 477, 153
Bacon, R., Accardo, M., Adjali, L., et al. 2010, Proc. SPIE, 7735, 773508
Benetti, S., Cappellaro, E., Mazzali, P. A., et al. 2005, ApJ, 623, 1011
Benetti, S., Meikle, P., Stehle, M., et al. 2004, MNRAS, 348, 261
Betoule, M., Kessler, R., Guy, J., et al. 2014, A&A, 568, A22
Biswas, R., Goobar, A., Dhawan, S., et al. 2022, MNRAS, 509, 5340
Blondin, S., Dessart, L., & Hillier, D. J. 2015, MNRAS, 448, 2766
Blondin, S., Dessart, L., & Hillier, D. J. 2018, MNRAS, 474, 3931
Blondin, S., Matheson, T., Kirshner, R. P., et al. 2012, AJ, 143, 126
Branch, D., Dang, L. C., Hall, N., et al. 2006, PASP, 118, 560
Brown, P. 2014, in Proc. of Swift: 10 Years of Discovery SWIFT 10 (Trieste: PoS), 125
Burns, C. R., Ashall, C., Contreras, C., et al. 2020, ApJ, 895, 118
Burns, C. R., Parent, E., Phillips, M. M., et al. 2018, ApJ, 869, 56
Burns, C. R., Stritzinger, M., Phillips, M. M., et al. 2011, AJ, 141, 19
Burns, C. R., Stritzinger, M., Phillips, M. M., et al. 2014, ApJ, 789, 32
de Vaucouleurs, G., de Vaucouleurs, A., Corwin, H. G. J., et al. 1991, Third Reference Catalogue of Bright Galaxies (New York: Springer)
Diamond, T. R., Hoeflich, P., Hsiao, E. Y., et al. 2018, ApJ, 861, 119
Dong, S., Katz, B., Kushnir, D., & Prieto, J. L. 2015, MNRAS, 454, L61
Drake, A. J., Djorgovski, S. G., Mahabal, A., et al. 2009, ApJ, 696, 870
Fakhouri, H. K., Boone, K., Aldering, G., et al. 2015, ApJ, 815, 58
Feindt, U., Kerschhaggl, M., Kowalski, M., et al. 2013, A&A, 560, A90
Filippenko, A. V., Richmond, M. W., Branch, D., et al. 1992b, AJ, 104, 1543
Filippenko, A. V., Richmond, M. W., Matheson, T., et al. 1992a, ApJL, 384, L15
Folatelli, G., Morrell, N., Phillips, M. M., et al. 2013, ApJ, 773, 53
Foley, R. J., Challis, P. J., Chornock, R., et al. 2013, ApJ, 767, 57
Foley, R. J., Hoffmann, S. L., Macri, L. M., et al. 2020, MNRAS, 491, 5991
Foley, R. J., Narayan, G., Challis, P. J., et al. 2010, ApJ, 708, 1748
Galbany, L., Anderson, J. P., Rosales-Ortega, F. F., et al. 2016, MNRAS, 455, 4087
Galbany, L., Ashall, C., Höflich, P., et al. 2019, A&A, 630, A76
Gall, C., Stritzinger, M. D., Ashall, C., et al. 2018, A&A, 611, A58
Gall, E. E. E., Taubenberger, S., Kromer, M., et al. 2012, MNRAS, 427, 994
Garavini, G., Folatelli, G., Nobili, S., et al. 2007, A&A, 470, 411
Hamuy, M., Folatelli, G., Morrell, N. I., et al. 2006, PASP, 118, 2
Hamuy, M., Phillips, M. M., Suntzeff, N. B., et al. 1996, AJ, 112, 2391
Hamuy, M., Phillips, M. M., Suntzeff, N. B., et al. 2003, Natur, 424, 651
Hicken, M., Garnavich, P. M., Prieto, J. L., et al. 2007, ApJL, 669, L17
Hoeflich, P., Hsiao, E. Y., Ashall, C., et al. 2017, ApJ, 846, 58
Hoeflich, P., & Khokhlov, A. 1996, ApJ, 457, 500
Höflich, P., Gerardy, C. L., Fesen, R. A., & Sakai, S. 2002, ApJ, 568, 791
Howell, D. A., Sullivan, M., Nugent, P. E., et al. 2006, Natur, 443, 308
Howerton, S. 2016, Transient Name Server Discovery Report, 2016-157, IAU Supernova Working Group
Hoyle, F., & Fowler, W. A. 1960, ApJ, 132, 565
Hsiao, E. Y., Burns, C. R., Contreras, C., et al. 2015, A&A, 578, A9
Hsiao, E. Y., Hoeflich, P., Ashall, C., et al. 2020, ApJ, 900, 140
Hsiao, E. Y., Marion, G. H., Phillips, M. M., et al. 2013, ApJ, 766, 72
Hsiao, E. Y., Phillips, M. M., Marion, G. H., et al. 2019, PASP, 131, 014002
Iben, I. J., & Tutukov, A. V. 1984, ApJS, 54, 335
J., & Iben, I. J. 1973, ApJ, 186, 1007
Jack, D., Baron, E., & Hauschildt, P. H. 2015, MNRAS, 449, 3581
Jensen, J. B., Blakeslee, J. P., Ma, C.-P., et al. 2021, ApJS, 255, 21
Jha, S., Kirshner, R. P., Challis, P., et al. 2006, AJ, 131, 527
Kasen, D. 2006, ApJ, 649, 939
Katz, B., & Dong, S. 2012, arXiv:1211.4584
Kelly, P. L., Hicken, M., Burke, D. L., Mandel, K. S., & Kirshner, R. P. 2010, ApJ, 715, 743
Khetan, N., Izzo, L., Branchesi, M., et al. 2021, A&A, 647, A72
Kochanek, C. S., Shappee, B. J., Stanek, K. Z., et al. 2017, PASP, 129, 104502
Kowalski, M., Rubin, D., Aldering, G., et al. 2008, ApJ, 686, 749
Krisciunas, K., Contreras, C., Burns, C. R., et al. 2017, AJ, 154, 211
Kushnir, D., Katz, B., Dong, S., Livne, E., & Fernández, R. 2013, ApJL, 778, L37
Lampeitl, H., Smith, M., Nichol, R. C., et al. 2010, ApJ, 722, 566
Leibundgut, B., Kirshner, R. P., Phillips, M. M., et al. 1993, AJ, 105, 301
Leloudas, G., Stritzinger, M. D., Sollerman, J., et al. 2009, A&A, 505, 265
Li, W., Filippenko, A. V., Chornock, R., et al. 2003, PASP, 115, 453
Li, W., Leaman, J., Chornock, R., et al. 2011, MNRAS, 412, 1441
Li, W. D., Qiu, Y. L., Qiao, Q. Y., et al. 1997, IAU Circ., 6661, 1
Livne, E. 1990, ApJL, 354, L53
López-Cobá, C., Sánchez, S. F., Anderson, J. P., et al. 2020, AJ, 159, 167
Lu, J., Ashall, C., Hsiao, E. Y., et al. 2021, ApJ, 920, 107
Marion, G. H., Höflich, P., Gerardy, C. L., et al. 2009, AJ, 138, 727
Matheson, T., Filippenko, A. V., Li, W., Leonard, D. C., & Shields, J. C. 2001, AJ, 121, 1648
Mazzali, P. A., Ashall, C., Pian, E., et al. 2018, MNRAS, 476, 2905
Mazzali, P. A., Chugai, N., Turatto, M., et al. 1997, MNRAS, 284, 151
Mazzali, P. A., Röpke, F. K., Benetti, S., & Hillebrandt, W. 2007, Sci, 315, 825
Modjaz, M., Li, W., Filippenko, A. V., et al. 2001, PASP, 113, 308
Nomoto, K. 1980, in Texas Workshop on Type I Supernovae, ed. J. C. Wheeler (Austin, TX: Univ. Texas), 164
Nomoto, K., Iwamoto, K., Nakasato, N., et al. 1997, NuPhA, 621, 467
Nugent, P., Phillips, M., Baron, E., Branch, D., & Hauschildt, P. 1995, ApJL, 455, L147
Nugent, P. E., Sullivan, M., Cenko, S. B., et al. 2011, Natur, 480, 344
Pastorello, A., Mazzali, P. A., Pignata, G., et al. 2007, MNRAS, 377, 1531
Pejcha, O., Antognini, J. M., Shappee, B. J., & Thompson, T. A. 2013, MNRAS, 435, 943
Perlmutter, S., Aldering, G., Goldhaber, G., et al. 1999, ApJ, 517, 565
Phillips, M. M. 1993, ApJL, 413, L105
Phillips, M. M. 2012, PASA, 29, 434
Phillips, M. M., Contreras, C., Hsiao, E. Y., et al. 2019, PASP, 131, 014001
Phillips, M. M., Lira, P., Suntzeff, N. B., et al. 1999, AJ, 118, 1766
Phillips, M. M., Phillips, A. C., Heathcote, S. R., et al. 1987, PASP, 99, 592
Phillips, M. M., Simon, J. D., Morrell, N., et al. 2013, ApJ, 779, 38
Phillips, M. M., Wells, L. A., Suntzeff, N. B., et al. 1992, AJ, 103, 1632
Piersanti, L., Gagliardi, S., Iben, Icko, J., & Tornambé, A. 2003, ApJ, 598, 1229
Poznanski, D., Prochaska, J. X., & Bloom, J. S. 2012, MNRAS, 426, 1465
Raiteri, C. M., Villata, M., & Navarro, J. F. 1996, A&A, 315, 105

Raskin, C., Timmes, F. X., Scannapieco, E., Diehl, S., & Fryer, C. 2009, MNRAS, 399, L156
Riess, A. G., Filippenko, A. V., Challis, P., et al. 1998, AJ, 116, 1009
Riess, A. G., Macri, L. M., Hoffmann, S. L., et al. 2016, ApJ, 826, 56
Rosswog, S., Kasen, D., Guillochon, J., & Ramirez-Ruiz, E. 2009, ApJL, 705, L128
Schlafly, E. F., & Finkbeiner, D. P. 2011, ApJ, 737, 103
Scolnic, D., Smith, M., Massiah, A., et al. 2020, ApJL, 896, L13
Scolnic, D. M., Jones, D. O., Rest, A., et al. 2018, ApJ, 859, 101
Shappee, B. J., Prieto, J. L., Grupe, D., et al. 2014, ApJ, 788, 48
Shappee, B. J., & Thompson, T. A. 2013, ApJ, 766, 64
Silverman, J. M., Foley, R. J., Filippenko, A. V., et al. 2012, MNRAS, 425, 1789
Simien, F., & Prugniel, P. 1997, A&AS, 126, 15
Smartt, S. J., Valenti, S., Fraser, M., et al. 2015, A&A, 579, A40
Stritzinger, M., Burns, C. R., Phillips, M. M., et al. 2010, AJ, 140, 2036
Stritzinger, M., & Leibundgut, B. 2005, A&A, 431, 423
Stritzinger, M., Leibundgut, B., Walch, S., & Contardo, G. 2006, A&A, 450, 241
Sullivan, M., Conley, A., Howell, D. A., et al. 2010, MNRAS, 406, 782
Szabó, G. M., Sárneczky, K., Vinkó, J., et al. 2003, A&A, 408, 915
Taubenberger, S. 2017, in The Extremes of Thermonuclear Supernovae, ed. A. W. Alsabti & P. Murdin (New York: Springer International), 317
Thompson, T. A. 2011, ApJ, 741, 82
Turatto, M., Benetti, S., Cappellaro, E., et al. 1996, MNRAS, 283, 1
Turatto, M., Piemonte, A., Benetti, S., et al. 1998, AJ, 116, 2431
van den Bosch, R. C. E., Gebhardt, K., Gültekin, K., Yıldırım, A., & Walsh, J. L. 2015, ApJS, 218, 10
van Kerkwijk, M. H., Chang, P., & Justham, S. 2010, ApJL, 722, L157
Webbink, R. F. 1984, ApJ, 277, 355
Wheeler, J. C., Höflich, P., Harkness, R. P., & Spyromilio, J. 1998, ApJ, 496, 908
Woosley, S. E., & Weaver, T. A. 1994, ApJ, 423, 371
Wyatt, S. D., Sand, D. J., Hsiao, E. Y., et al. 2021, ApJ, 914, 57
Yamanaka, M., Kawabata, K. S., Kinugasa, K., et al. 2009, ApJL, 707, L118
Yaron, O. 2017, Transient Name Server Classification Report, 2017-705, IAU Supernova Working Group